

Intense and localized export of selected marine snow types at eddy edges in the South Atlantic Ocean

Alexandre Accardo¹, Rémi Laxenaire^{4,5,6}, Alberto Baudena¹, Sabrina Speich^{3,4}, Rainer Kiko², Lars Stemmann^{1,7}

¹Sorbonne Université, CNRS, Laboratoire d'Océanographie de Villefranche, UMR 7093 LOV, Villefranche-sur-Mer, France

²GEOMAR Helmholtz Center for Ocean Research Kiel, Germany

³Ecole Normale Supérieure, PSL Research University, France

⁴UMR 8539 Laboratoire de météorologie dynamique (LMD), France

⁵UMR 8105 Laboratoire de l'Atmosphère et des Cyclones, Saint-Denis de La Réunion, France

⁶Center for Ocean-Atmospheric Prediction Studies, Florida State University, Tallahassee, FL, United States

⁷Institut Universitaire de France (IUF), France

Correspondence to: Alexandre Accardo (alexandre.accardo@imev-mer.fr)

Abstract

The Biological Carbon Pump (BCP) comprises a wide variety of processes involved in transferring organic carbon from the surface to the deep ocean. This results in long-term carbon sequestration. Without BCP, atmospheric CO₂ concentrations would be around 200 ppm higher. This study reveals that ocean dynamics at mesoscale and submesoscale could have a major impact on particulate organic matter (POM) vertical distribution. Our results suggest that intense submesoscale frontal regions, such as those between mesoscale eddies, could lead to an important accumulation and transport of particulate organic matter (POM) from the mixed layer depth (MLD) down to the mesopelagic zone. To reach these conclusions, a multifaceted approach was applied. It included in-situ measurements and marine snow images from a BGC Argo float equipped with an Underwater Vision Profiler (UVP6), satellite altimetry data, and Lagrangian physics diagnostics. We focused our study on three intense features in marine snow distribution observed during the 17-month long float mission in the Cape Basin, southwest of Africa. These features were located in the frontal region between mesoscale eddies. Our study suggests that a particle injection pump induced by a frontogenesis-driven mechanism has the potential to enhance the effectiveness of the biological pump by increasing the depth at which carbon is injected into the water column. This work also emphasizes the importance of establishing repeated sampling campaigns targeting the interface zones between eddies. This could improve our understanding of the mechanisms involved in the deep accumulation of marine snow observed at eddy interfaces.

a supprimé: Massive

a mis en forme : Français

a mis en forme : Français

a supprimé: The open ocean plays a critical role in mitigating climate change by sequestering carbon dioxide (CO₂) from the atmosphere for long periods of time. This carbon storage occurs over decades to millennia and relies on the physical pump that transports cold, dense, and DIC-rich waters to the deep ocean, as part of the ocean's overturning circulation, and the biological carbon pump (BCP). The BCP encompasses a wide range of processes, from the fixation of atmospheric CO₂ by phytoplankton activity to carbon sequestration in the deep ocean. Atmospheric CO₂ concentrations would be about 200 ppm higher than in a world without biology, and the global climate would be much warmer by default. This study highlights the idea that BCP efficiency is enhanced by the ocean dynamics at mesoscale and submesoscale. In fact,

a supprimé: o

a supprimé: depths of about 600 meters

46 1 Introduction

47 The open ocean plays a critical role in mitigating climate change by storing carbon dioxide (CO₂) away from the atmosphere
48 for long periods of time (Boyd et al., 2019). This carbon storage occurs over decades to thousands of years and relies on two
49 well-established mechanisms that create a gradient of dissolved inorganic carbon (DIC) between the surface and deep regions
50 of the ocean and enhances DIC concentrations at depth. These mechanisms are known as the biological pump and the solubility
51 pump (or physical pump). The solubility pump transports cold, dense, and DIC-rich waters to the deep ocean, as part of the
52 ocean's overturning circulation, primarily in high-latitude regions (Sarmiento and Gruber, 2006). The biological carbon pump
53 (BCP), on the other hand, involves the export of particulate organic carbon (POC) from surface waters below the euphotic
54 depth, and operates worldwide. The BCP encompasses a wide range of processes, from the fixation of atmospheric CO₂ by
55 phytoplankton activity, to carbon sequestration into the deep ocean (Le Moigne, 2019). The BCP contributes also to
56 approximately 90% of the dissolved inorganic carbon (DIC) gradient between surface and deep ocean (Boyd et al., 2019).
57 Without the BCP atmospheric concentrations of the greenhouse gas CO₂ would be approximately 200 ppm higher than in a
58 world without biology (Maier-Reimer et al. 1996) and the global climate would be much warmer by default.

59 A key component of the BCP is the biological gravitational pump (BGP). The BGP is the process by which large and/or dense
60 aggregates of POC sink due to gravity. Large particles of POC (> 500 μm), also called marine snow, can consist of aggregated
61 phytoplankton cells such as diatoms, different types of aggregates resulting from coagulation processes (Le Moigne, 2019),
62 and zooplankton activity, such as phytoplankton grazing and faecal pellet egestion (Turner, 2015). This mechanism is
63 estimated, through empirical and food web models, to export about 3 to 10 Pg of carbon per year below the euphotic zone or
64 100 meters depth depending on the study (Dunne et al., 2005; Henson et al., 2012; Siegel et al., 2014; Bisson et al., 2020). The
65 speed at which surface aggregates sink to the deep ocean depends on their individual sinking rates, which are influenced by
66 their combined morphological (size, porosity, etc.) and chemical properties (ratio of organic versus mineral, mineral type, etc.)
67 (Stemmann et al., 2004; Cael et al., 2021; Trudnowska et al., 2021; Soviadan et al., submitted). Laboratory experiments have
68 estimated that the sinking velocity of marine snow range from a few meters to several hundred meters per day (Shanks and
69 Trent, 1980; Azetsu-Scott and Johnson, 1992; Ploug et al., 2008; Laurenceau-Cornec et al., 2015; Cael et al., 2021) and, in a
70 few cases, from in situ imaging time series (Alldredge and Gotschalk, 1988; Stemmann et al., 2002; Trudnowska et al., 2021;
71 Soviadan et al., 2024). In situ imagery has proven to be a valuable tool for estimating sinking speeds. This can improve our
72 understanding of particle dynamics, which affect the BGP.

73 Another important component of the BCP that can occur concurrently with the BGP, are the particle injection pumps (PIPs).
74 These consist of the export of carbon mediated by plankton migrations or physical vertical movement and can also play a
75 significant role in the ocean's capacity to store carbon. PIPs encompass a variety of mechanisms, temporal-spatial scales, and
76 geographical extent, and can affect all types of particles in the water column. They typically transport particles below the
77 euphotic zone. Depending on the specific injection mechanism, PIPs can reach depths greater than 1000 m (Boyd et al. 2019).

a supprimé: particulate organic carbon (

a supprimé:), typically produced by phytoplankton activity, sink under gravity

a supprimé: POC

a supprimé: (for particles >500μm),

a supprimé:

a supprimé: faecal pellets (Turner, 2015)

a supprimé: This mechanism is estimated to export about 6 Pg of carbon per year below the mixed layer depth (MLD; Boyd et al., 2019)

a supprimé: rate

a supprimé: s

a supprimé: (Stemmann et al., 2004; Cael et al., 2021).

a supprimé: Sinking rates of different types of marine snow types have been estimated to range from 10 to 100 m d⁻¹ from laboratory experiments (Shanks and Trent, 1980; Azetsu-Scott and Johnson, 1992) and, in a few cases, from in situ imaging time series (Alldredge and Gotschalk, 1988; Stemmann et al., 2002; Trudnowska et al., 2022).

a supprimé: In situ imaging of marine snow allows us to observe the change in size and morphology of aggregates as they progress through the ocean interior. This can improve our understanding of particle dynamics and, hopefully, their sinking rates, which affect the BGP.

a supprimé: , from those suspended in the water column to sinking particles

104 The physical processes that make up the PIPs include subduction resulting from the mixed-layer shallowing (referred to as the
105 mixed-layer pump), subduction caused by the large-scale ocean circulation over distances of 100-1000 km (referred to as the
106 large-scale subduction pump), and subduction mediated by mesoscale (10-100 km, few weeks to several months) to
107 submesoscale (100 m to 10 km, hours to days) ocean dynamics (Thomas et al., 2008; McWilliams, 2016).

a supprimé: Due to their dynamic nature, which includes physical transport or the patchy distribution of animals, the interaction between the vertical and horizontal components of PIPs, as well as their temporal scales, can vary significantly (Boyd et al., 2019).

108 In particular, the influence of mesoscale eddies on particle production, aggregation and export (Stemmann et al., 2008 ; Guidi
109 et al., 2012 ; McGillicuddy, 2016 ; Stuckel et al., 2017) is a very active area of research because these structures are ubiquitous
110 in the global ocean and are the largest source of ocean variability (Stammer, 1997; Wunsch, 1999). For example, spatial
111 patterns of particles, differentiated by size, have been shown to be associated with anticyclonic circulation (Gorsky et al., 2002;
112 Waite et al., 2016). Upwelling at eddy's interfaces can enhance phytoplankton productivity and particle production (Shih et
113 al., 2020) while downwelling, contributes to oblique transport of dissolved, and particulate (both sinking and suspended)
114 carbon to depth (Stemmann et al., 2008; Guidi et al., 2012) in a process called the Eddy Subduction Pump (ESP; Omand et al.
115 2015). Vertical transport has been suggested to be increased by sub-mesoscale vertical velocities associated with fronts (Guidi
116 et al., 2007). Understanding the mechanisms associated with physical-biological biogeochemical interaction is challenging due
117 to the transient nature of the underlying processes. Therefore, it is essential to employ multidisciplinary approaches, including
118 in situ observations, to elucidate these intricate phenomena (McGillicuddy, 2016).

a supprimé: to submesoscale (1-10 km, hours to days) ocean dynamics.

a supprimé: (McGillicuddy, 2016)

119 This work is based on the deployment of a new prototype of BGC Argo float (part of the Argo international program:
120 <https://argo.ucsd.edu>) equipped with an Underwater Vision Profiler 6 (UVP6; Picheral et al., 2022) and several physical-
121 biogeochemical sensors in the Southeast Atlantic Ocean. The float was deployed in the Cape Basin, a region southwest of
122 Africa, known for its intense eddy activity, which is mainly controlled by a complex interaction between the Benguela
123 Upwelling, the Agulhas Current System and the South Atlantic Current (Richardson et al., 2003; Boebel et al., 2003). The
124 float was recovered after one year of operation and the collected images were analyzed and classified into plankton categories
125 and morphological types of marine snow (Trudnowska et al., 2022). Hydrological and particle data collected by the float were
126 then combined with satellite altimetry to identify frontal structures and mesoscale eddies (Chaigneau et al., 2009; Laxenaire et
127 al., 2018; 2019; 2020; 2024). Based on recurrent observations of marine snow concentration "hot spots" at mesopelagic depth
128 during the productive season, we discuss the role of horizontal and vertical circulation at fronts on marine snow production
129 and export to the deep sea.

a supprimé: They also play an important role in the vertical distribution of water mass properties as they are associated with upwelling and downwelling. Upwelling results in the transport of nutrients to the surface mixed layer which normally enhances productivity. Downwelling results in the physical transport of dissolved, and particulate (both sinking and suspended) carbon to depth.

a supprimé: The aim of the present work is to understand how frontogenesis mechanisms induced by mesoscale activity coupled with the gravitational carbon pump can lead to the rapid accumulation of diverse particulate matter ranging from 5 μ m to 16 mm in size at depths exceeding 600 meters.

130 2 Material and Methods

131 1.1 Observing strategy

132 During the SO283 cruise, a BGC Argo float (WMO: 6903095) was deployed, from the RV Sonne, on April 14, 2021, in a
133 cyclonic eddy in the southeastern region of the Atlantic Ocean, near the Benguela upwelling system at 33.0978°S and

154 13.8673°E (Fig. 1.A). The float remained within the eddy for about 5 months. ~~During this period, the eddy merged with another~~
155 ~~cyclone (Baudena et al., 2023), until it disappeared from satellite altimetry maps probably due to subduction (Ioannou et al.,~~
156 ~~2022). A detailed analysis of this timeframe of the dataset is provided in Baudena et al., (2023).~~ It then sampled different
157 mesoscale features within the region, and after a sampling period of about 1.5 years, it was retrieved by the S.A. Agulhas II
158 on September 19, 2022. During its deployment, the float completed a total of 183 profiles, the majority of which were acquired
159 from the surface down to 600- or 1000-meter depth.

160 1.2 Environmental data

161 The float was equipped with several sensors to quantify seawater properties along the water column. The float was
162 instrumented with pressure (DRUCK_2900PSIA, SN: 11587115), temperature and salinity sensors (SBE41CP_V7.2.5, SN:
163 13100) to measure the hydrological water properties. The biogeochemical properties were measured with oxygen
164 (AANDERAA_OPTODE_4330, SN: 3489), fluorescence and backscattering (700 nm) sensors (ECO_FLBB_2K, SN: 6310).
165 All the BGC Argo data that were used in this work, are made freely available by the International Argo Program
166 (<https://fleetmonitoring.euro-argo.eu/float/6903095>). Before analysis, some derived variables were calculated based on a
167 Python implementation of the Gibbs SeaWater (GSW) Oceanographic Toolbox of TEOS-10 (<http://www.teos-10.org/>). Firstly,
168 Absolute Salinity (SA) was computed from Practical Salinity (PSAL) and pressure (dbar) measurements and Conservative
169 Temperature (CT, °C) was computed from in-situ Temperature (T, °C). These two variables were then used to calculate the
170 Potential Density (kg.m^{-3}) with a reference pressure of 0 dbar (Roquet et al., 2015). Regarding the oxygen parameter, the
171 Apparent Oxygen Utilization (AOU, $\mu\text{mol.kg}^{-3}$) was computed as the difference between the oxygen concentration expected
172 at equilibrium with air and the in-situ oxygen concentrations. The expected oxygen concentration was computed from
173 solubility coefficients derived from the data of Benson and Krause (1984), as fitted by Garcia and Gordon (1992). Finally, the
174 mixed layer depth (MLD), which is the upper part of the water column where salinity, temperature, and density remain
175 vertically constant, was detected following De Boyer Montégut (2004). A reference value for density was taken at 5 dbar and
176 the water column was considered to be mixed until the depth at which density deviates from this reference by more than 0.03
177 kg.m^{-3} .

178 1.2 Living and non-living particle data

179 1.1.1 Small phytoplanktonic and bulk particles

180 To estimate chlorophyll-a concentrations emitted by phytoplanktonic cells, the float was equipped with a fluorescence sensor
181 (ECO_FLBB_2K, SN: 6310). The backscattering (700 nm) sensor (ECO_FLBB_2K, SN: 6310) was used to quantify the
182 amount of all particles (including detritus and phytoplankton). The backscattering coefficient signal (*bbp*) was decomposed to
183 extract the signal of small particles (*bbsr*) from the raw signal which also contained spikes triggered by rare large aggregates
184 passing in the flow field. This was done by applying the method proposed by Briggs et al., 2020 (see supplementary materials)

a supprimé: .

a supprimé: (Baudena et al. 2023, preprint)

a supprimé: the eddy

a supprimé: because

a supprimé: of

a supprimé: in the ocean interior

a supprimé: labile and refractory

192 that decomposes the backscattering signal into its baseline (as a proxy of small particles, *bbsr*) and intermittent pulses (as
193 proxy of larger aggregates). The *bbsr* signal represented the distribution of particles between 5 to 20 μm .

194 1.2.2 Underwater Vision Profiler 6 (UVP6-LP)

195 The float was also equipped with an in-situ camera, the Underwater Vision Profiler 6 Low-Power (UVP6-LP, SN: 000101)
196 specifically designed to be deployed on autonomous platforms. The UVP6 detects and measures the size (from 0.102 to 16.40
197 mm in Equivalent Spherical Diameter, ESD) of zooplankton and various organic/biogenic matter such as marine snow and
198 fecal pellets. Thanks to the float recovery, images of objects $>500 \mu\text{m}$ could be retrieved as well and therefore, taxonomic
199 identification of macrozooplankton and large particle classification could be conducted on the Ecotaxa platform
200 (<http://ecotaxa.obs-vlfr.fr>). Taxonomic classification was initially assisted by a CNN (Convolutional Neural Network)
201 algorithm to extract descriptive features from the images. From these, the taxonomic group of each image was predicted using
202 a Random Forest algorithm. Then, living organisms' predictions have all been manually validated by taxonomic experts. All
203 the images used during this work can be found here: <https://ecotaxa.obs-vlfr.fr/prj/8801>. A more detailed description of the
204 UVP6-LP can be found in Picheral et al., 2022.

205 1.2.3 A broad size classification of particles (MiP and MaP)

206 To conduct a community analysis of marine snow and examine their spatio-temporal distribution, we applied a rough size
207 classification on raw size- spectra data ($>100 \mu\text{m}$) provided by the UVP6 (without any plankton identification). In this case
208 the assumption was made that zooplankton represents only a small fraction of objects sampled by the UVP6 (14.5% of images)
209 compared to particles (85.5%). Hence, we consider its contribution as neglectable for this purpose. Then, all size-spectra were
210 divided into two sub-classes: MiP (Micrometric Particles) and MaP (Macroscopic Particles). MiP concentrations were obtained
211 by integrating the concentrations overall size classes between 0.1- and 0.5-mm. MaP concentrations were computed exactly in
212 the same way but considering all size classes between 0.5- and 16-mm. The 0.5 mm threshold was used as detrital aggregates
213 $> 0.5 \text{ mm}$ are considered marine snow (i.e., aggregates, Alldredge and Gotschalk, 1988) and was chosen for visualization
214 purposes. However, the count/size measurements of the objects seen by the UVP6 contain zooplanktons and it is not possible,
215 from the images, to determine whether an object smaller than 0.5 mm is a living organism or detritus due to the limited
216 resolution. As a result, the MiP and MaP signals could be influenced by zooplankton abundances. However, the proportion of
217 living organisms to the total particle counts (ESD $> 500\mu\text{m}$) are usually smaller than 10% (Stemmann and Boss, 2012).

218 Organic carbon content of MiPs and MaPs was calculated assuming that particle mass can be estimated using an empirically
219 derived relationship for marine aggregates (Alldredge, 1998; Kriest, 2002 reference 2a of Table 1). Assuming a
220 carbon:nitrogen ratio of 106:16, this yields an expression for the carbon content of a particle in a given size class characterized
221 by its diameter ESD (in μm). Moreover, this formula is dedicated to estimate POC content of miscellaneous marine snow,
222 including components such as fecal pellets. Multiplying the carbon content with the particle number in this size class (in

a supprimé: POC (Particulate Organic Carbon),

a supprimé: .

225 particles.m⁻³), and integrating over the MiP and MaP size classes, respectively, we obtain the total POC content (mgC.m⁻³) for
226 MiPs and MaPs.

227 Our study suggests the presence of vertical velocities within the water column which could significantly influence the marine
228 snow distribution (MiPs and MaPs) at depth. The literature provides various methods for estimating POC fluxes from imaging
229 devices. However, these approaches are based on particle size, sinking speed, and carbon content relationships which do not
230 include the influence of physical processes such as water masses vertical movement. Therefore, a simple POC fluxes estimates
231 from particle size would not accurately represent the actual fluxes in our study area. Furthermore, we couldn't disentangle the
232 contributions of particle sinking speeds from the vertical displacement of the water mass. Given these limitations, we chose
233 not to provide flux estimates.

234 The raw data corresponding to this section can be found on the Ecopart platform ([https://ecopart.obs-vlfr.fr, project:](https://ecopart.obs-vlfr.fr/project:uvp6_sn000101lp_2021_WMO6903095_recovery)
235 uvp6_sn000101lp_2021_WMO6903095_recovery).

236 **1.2.4 Unsupervised morphological classification of marine snow**

237 To better characterize the marine snow dynamics, an unsupervised classification method was used, following the previous
238 study on particle dynamics in the Arctic Ocean (Trudnowska et al., 2021). This provides information on particle size, shape,
239 gray level, and heterogeneity. This method allows one to classify rapidly and efficiently particle images in objective categories.
240 In summary, firstly, zooplankton and detrital particle images were separated, by manual validation and treated independently.
241 After this separation, a PCA was performed on morphological traits of the detrital particle images. Those specific traits
242 represented their size (e.g., area, perimeter), shade intensity (e.g., mean/median gray level), shape (e.g., symmetry, elongation),
243 and structure (i.e., homogeneity or heterogeneity, mostly based on the variability in gray level). To obtain a normal distribution
244 for each variable, extreme values (in that they were below or above the first and 95th percentile) were removed and each
245 variable was transformed by the Yeo-Johnson transformation (Yeo, 2000). This PCA led to the creation of a morphospace in
246 which each particle image can be located based on their morphological features. Then, a K-means clustering was performed
247 on this new morphospace using the first five principal components. The number of clusters, “k”, was set to four. This specific
248 number, after several simulations, was chosen because it conducted the best partitioning with four clearly different groups of
249 particle morphology.

250 Finally, the concentration (nb.m⁻³) of each morphotype was computed by multiplying the number of particles found in each
251 cluster and depth bin by the volume sampled by the UVP6. To study their spatio-temporal distributions, group concentrations
252 were interpolated according to depth and time with a resolution of 5 meters and one day respectively.

253 Since some groups in the morphospace partially overlap (Fig. 5_B), potentially affecting the quality of the classification, a
254 further selection process was implemented. This involved calculating the Euclidean distance between individual particle
255 images and their respective cluster centers. Subsequently, for each group, the first quartile of the Euclidean distance distribution

256 was computed, and only individuals with a distance smaller than the first quartile were included in the selection. The
257 concentrations of the different morphotypes shown in figure 6 correspond to those of these 'exclusive members'. Objects with
258 a too large distance (out of the first quartile) were not included in the further analysis.

259 1.2.5 Selection of profiles corresponding to deep massive exports

260 To characterize in an objective way significant changes in the deep marine snow spatio-temporal distribution, the Sequential
261 T-test Analysis of Regime Shifts (STARS) method was used (Rodionov, 2004). This method, based on the Student's t-test2,
262 analyses a dataset in a sequential manner. It compares each new observation with all the entries in the current 'regime' or group.
263 If an entry significantly deviates from the average of that regime, it is marked as a potential 'shift point'. The algorithm then
264 tests whether this detected shift is persistent over time. To characterize significant changes in the water column, marine snow
265 concentrations were integrated, for each UVP6 profile, between 150 and 600 meters. Then, profiles detected in each significant
266 'shift' were selected and considered as belonging to (or 'inside') those features in marine snow distribution (see Fig. S1).
267 Afterward, to compare the aggregates distribution outside and inside each feature, profiles one month before and one month
268 after each feature were selected and merged, providing the mean of particle concentrations 'outside' each feature. The same
269 protocol was applied to study the morphotype proportions according to depth. The latter were computed in four depth layers,
270 between 0-100, 100-300, 300-600 and 600-1000 meters to see the evolution of the morphotypes relative abundance overall the
271 water column.

272 1.2.6 Eddy subduction detection

273 To compare our findings with the literature, we applied the algorithm proposed by Llorc et al., 2018 to detect ESP events from
274 AOU and spiciness anomalies derived from BGC-Argo float data. Spiciness was defined as in Flament, 2002 and allows
275 differentiating water masses with distinct thermohaline properties but with similar density. Then, we compared each profile's
276 3-bin smoothed values to a 20-bin average to detect anomalies for both AOU and spiciness. An event was classified as
277 subduction-driven only if AOU and spiciness anomalies occurred at the same depth, which helped differentiate subduction
278 effects from horizontal mixing. Thresholds of AOU anomaly < -8 $\mu\text{mol/kg}$ and spiciness < -0.05 were set to detect these kinds
279 of events. Finally, we compared the ESP occurrence with the export features spatial distribution detected with the STARS
280 method. We also considered calculating vertical velocities according to Siegelman et al. (2020), but the temporal resolution of
281 our data was not sufficient to enable this (pers. communication L. Siegelman).

282 1.3 Satellite data and the TOEddies algorithm

283 To identify mesoscale eddies, we implemented the TOEddies algorithm (The Ocean Eddy Detection and Tracking Algorithm,
284 Laxenaire et al., 2024). TOEddies is based on the identification of mesoscale eddies as closed contours of Sea Surface Height
285 (SSH) surrounding an extremum. This relies on the principle that in a geostrophic balance, SSH isolines align with current
286 streamlines. As a result, a maximum (minimum) SSH that is surrounded by a closed circulation is classified as an anticyclonic

a supprimé: Subsequently, for each group, the first quartile distance was computed, and only individuals with a distance smaller than the first quartile were included in the selection. These 'new' members (called 'exclusive members') were then used as indicators to see potential differences in the distribution pattern of each morphotype.

a mis en forme : Titre 3

a supprimé: 2018

294 (cyclonic) eddy. To track the eddies over time, the algorithm takes advantage of the fact that daily eddy displacements are
295 small compared to their dimensions, resulting in overlapping areas between successive days. This methodology allows the
296 derivation of trajectories and the detection of events where eddies merge or split, providing a mechanism for tracing the origin
297 of sampled water masses which is a critical component for the objectives of this study.

298 For the purposes of this study, the TOEddies algorithm was applied to the Absolute Dynamic Topography (ADT, a proxy for
299 SSH) and its associated with geostrophic currents. These 1/4 gridded daily maps are produced by Ssalto/Duacs and distributed
300 by the Copernicus Marine Environment Monitoring Service (<http://marine.copernicus.eu/>) in the version released in April 2018
301 (DT18; Pujol et al., 2016; Ballarotta et al., 2019). Each identified eddy was characterized by two radii associated to the two
302 eddy boundaries defined in TOEddies: the outermost contour (R_{out}), and the contour with the maximum averaged geostrophic
303 velocities ($R_{V_{max}}$ and associated velocity V_{max}).

304 Eddies identified by the algorithm were collocated with float profiles (Chaigneau et al., 2011; Laxenaire et al., 2019; 2020).
305 This allows us to categorize the profiles according to whether they sampled a cyclone, an anticyclone, a region outside of the
306 influence of mesoscale eddies, or an area at the interface of two eddies. The application of TOEddies to ADT maps, coupled
307 with the collocation of detected eddies with Argo profiles, has proven to be a successful combination for exploring eddy
308 dynamics in the southeast Atlantic (Laxenaire et al., 2019, 2020; Ioannou et al., 2022; Baudena et al., 2023).

309 1.4 Lagrangian diagnostics

310 Several Lagrangian diagnostics have been computed at the location of each profile using satellite-derived currents and
311 environmental variables. First, for each station (i.e., profile location), a region was defined as representative of the water parcel
312 sampled by the float. In this study, this region was a circular neighborhood with a radius r of 0.1° around each profile location.
313 This distance allowed us to smooth the satellite uncertainties and has been used in previous studies (Chambault et al., 2019;
314 Baudena et al., 2021; Ser-Giacomi et al., 2021; Fabri-Ruiz et al., 2023). This circular shape was then filled with virtual particles
315 (nearly 300) separated by 0.01° . Then, for each virtual particle, a given Lagrangian diagnostic was computed (detailed below).
316 This resulted in about 300 values for each sampling station. These have been averaged, leading to a value of a given Lagrangian
317 diagnostic for each profile. The velocity field we used have been derived from both altimetry and delayed-time model
318 assimilation data and includes both the geostrophic and the Ekman components (Copernicus CMEMS product MULTIOBS
319 GLO PHY REP 015 004-TDS). It has been used backward in time to advect each virtual particle (within the representative
320 water parcel) from the profile day until an advective time (τ). Different τ values were used, ranging from 5 to 45 days. Hence,
321 for each profile, each diagnostic has been calculated using different advective times. The first diagnostic we implemented was
322 the Finite-Time Lyapunov Exponent (FTLE, days⁻¹; Shadden et al., 2005). By construction, intense FTLE values (typically
323 disposed in filament shapes) are found at the edge between two water masses that have been widely separated in the preceding
324 days. As these two water masses come from distant locations, they are likely to share different hydrological characteristics,
325 such as temperature, primary production or biological activity (d'Ovidio et al., 2010; Haller, 2015; Lehahn et al., 2018). For
326 these reasons, FTLE is useful to identify oceanic fronts and can be considered as proxies for water masses convergence and

a supprimé: the origin of sampled water masses—a critical component for the objectives of this study

a mis en forme : Indice

a supprimé: R_{max}

a mis en forme : Indice

a supprimé: The first diagnostic we implemented was the Finite-Time Lyapunov Exponents (FTLE, days⁻¹; Shadden et al., 2005). ...

333 thus, possibly, associated vertical downwelling (McWilliams, 2016), FTLEs were computed as in Shadden et al., (2005), with
334 an initial separation of 0.1° . We implemented as a second diagnostic the Lagrangian chlorophyll-a ($\text{mg}\cdot\text{m}^{-3}$), which is the mean
335 chlorophyll content calculated along the backward virtual particle trajectory. This diagnostic determines whether the seawater
336 parcel sampled at a profile location was rich in chlorophyll in the preceding days. For the chlorophyll, we used the delayed-
337 time satellite product “OCEANCOLOUR GLO BGC L4 MY 009 104-TDS” provided by CMEMS Copernicus website (0.25°
338 resolution, provided daily).

a supprimé: This metric is useful for identifying fronts. A front is defined as a physical barrier that separates two adjacent water masses that have been widely separated in the preceding days and are likely to have different hydrographic properties....

a supprimé: ¶

339 2 Results

340 2.1 Circulation and water mass spatio-temporal distribution

341 The lateral variability in thermohaline properties (Fig. 2) is driven by mesoscale eddies and submesoscale features, which carry
342 distinct signatures and interact dynamically, creating spatio-temporal heterogeneity in water masses. Visual inspection of the
343 TOEddies algorithm results, coupled with analysis of hydrological data provided important information about the history and
344 origin of the water masses sampled by the float. In the following, we separate the life history of the float trajectory in different
345 periods. During April to October 2021 (fall and winter), the float was trapped within a cyclonic eddy shed from the southern
346 Benguela upwelling front (Baudena et al., 2023, preprint). During this period, temperature, salinity, and density were relatively
347 stable. Figure 2 shows that the MLD varied between near-surface depths and 200 m. Analysis of the AOU time series shows
348 predominantly weak positive or even negative values only above the MLD (Fig. 2.F). Regarding the FTLE time series, values
349 remained low compared to the entire time series (less than 0.25 days^{-1}) except around August 2021 when the targeted eddy
350 merged with another Benguela Upwelling cyclone (0.45 days^{-1}). Overall, the float remained near the center of the cyclonic
351 eddy, which explains the low FTLE values. After the merging, the float continued to move within the new cyclonic structure.
352 This cyclonic eddy merged again (in early October 2021) with an Agulhas cyclone that formed along the Agulhas Bank, the
353 southern shelf-edge of Africa (Penven et al., 2001; Lutjeharms et al., 2003). This type of cyclone originates from the southern
354 African continental slope from barotropic instabilities and enters the ocean interior at the northern edge of the Agulhas Current
355 Retroflection (Duncombe Rae, 1991) with very different hydrographic characteristics (warmer and saltier water masses,
356 Giulivi and Gordon, 2006) compared with the Benguela upwelling cyclones.

a supprimé: The study area exhibits significant environmental variability, in terms of water masses and their spatio-temporal variability in relation to intense mesoscale activity (Fig. 2).

357 After exiting the cyclone, the float remained within its periphery. In mid-October, the float was at the interface between the
358 cyclone and an anticyclonic eddy. Then, the float moved southward until May 2022. The water column was more stratified
359 and characterized by a shallower MLD (typical for spring and summer). During this period, two phases of the life history of
360 the float can be identified. During the first phase, warmer and saltier waters were observed between 200 and 800 m depth.
361 These waters clearly originate from Agulhas Current water masses, very likely originating from an injection in the region of
362 the Agulhas rings generated at the Agulhas Current Retroflection (Laxenaire et al., 2018). The second phase is characterized
363 by colder and fresher water masses. Indeed, between January and March 2022, the float crossed the Subantarctic front and

374 continued to move southward along the edge of an Agulhas ring, a relatively old Agulhas cyclone, as well as a Subantarctic
375 Front cyclone. Finally, in April 2022, the float passed next to another Subantarctic Front cyclone, which could explain the
376 colder and less salty water masses during this period. Moreover, specific patterns in the AOU and the density time series are
377 also observed during the transition between these two phases. Indeed, the AOU time series shows smaller values (close to 0
378 $\mu\text{mol.m}^{-3}$) at depths between 200 and 1000 m. The latter are also associated with important horizontal isopycnal variations
379 (steep slopes), reaching depths close to 900 m and coinciding with high FTLE values (above 0.45 days^{-1}).

380 The final period spans May to September 2022 and is marked by three high-intensity mesoscale features that influence the
381 water column down to about 800 to 1000 m depth. These features are characterized by a deeper MLD and the presence of
382 much warmer and saltier water masses all over the water column. The AOU time series shows a strong signal during this
383 period, with negative values observed at depths around 800 m. This period was also characterized by intense FTLE values
384 throughout. The TOEddies analysis showed that the float profiled different cyclones and anticyclones during this period.

385 In summary, during its deployment, the float sampled water masses with significantly different hydrological characteristics
386 and from multiple geographical zones. At this stage, one of the main results to keep in mind is that the float sampled interface
387 zones between anticyclonic and cyclonic structure. Overall, these observations highlight the dynamic nature of the study area,
388 characterized by contrasting water mass properties and their temporal variations throughout the year.

389 2.2 Spatio-temporal distribution of marine snow during the survey

390 From April to October 2021 (Fall and Winter), surface chlorophyll-a concentrations and the *bbsr* coefficient remained
391 relatively low (Fig. 2.E.F). Afterwards, a significant change occurred between the end of October 2021 and May 2022 (Spring
392 and Summer). This period coincided with the seasonal production of phytoplankton, as evident in the chlorophyll-a
393 concentration time series. **Also, a noticeable increase in the *bbsr* coefficient indicates greater concentrations of small particles
394 in the surface (Fig. 2.E).** Moving forward to the period between May and September 2022, there was a noticeable decline in
395 chlorophyll-a concentration. Consequently, weaker concentrations were observed at the surface, and the *bbsr* coefficient was
396 also reduced. In general, the spatio-temporal dynamics of MiP and MaP exhibit notable differences (Fig. 3). MiPs were
397 generally more abundant than MaPs, ranging between $1.5\text{-}7.5 \text{ part.L}^{-1}$, while MaP concentrations ranged from 0 to 1.6
398 part.L^{-1} (Fig. 3). Both types of particles displayed higher mean concentrations above the MLD than below. MiP were
399 consistently present throughout the float deployment, with a slightly higher abundance observed between October 2021 and
400 May 2022. Conversely, the distribution pattern of MaPs differed. Their concentration was relatively low from the beginning
401 of the time series until October 2021. Subsequently, their surface abundance significantly increased during the phytoplankton
402 production period between the end of October 2021 and May 2022. Overall, these observations highlight the distinct spatio-
403 temporal dynamics of MiP and MaP. A key result in the marine snow spatial distribution is that three different "columns" of
404 increased particle concentration (in particular MaPs) were observed between the surface down to 600 meters. These features

a supprimé: There was also an observable increase in the concentration of small, labile, and refractory particles in the surface, as reflected by the *bbsr* coefficient (Fig. 2.E).

408 lasted for approximately a month. The first one took place between October 8 and 23, 2021, the second one occurred from
409 November 25 to December 22, 2021, and finally, the last one spanned approximately between March 3 and April 28, 2022.

410 2.3 Spatio-temporal distribution of MaP morphological groups during the survey

411 The unsupervised clustering method led to the identification of four morphotypes distinguished by their size, circularity,
412 brightness, and homogeneity (Fig. 5.A.B). The first morphotype was characterized by small, dark, and predominantly circular
413 particles. The second morphotype comprised elongated objects with varying degrees of brightness. The third morphotype
414 consisted of bright, fluffy, and diverse marine snow particles. The fourth morphotype encompassed larger marine snow
415 particles, often with the form of aggregated structures with some heterogeneity. All the identified morphotypes were
416 predominantly found in the surface layer. Specifically, the elongated particles (Fig. 6.B) exhibited a distinct concentration
417 increase from late September 2021, maintaining a stable abundance until early May 2022. Before and after this period, their
418 presence was considerably smaller. Additionally, these elongated particles displayed a strong positive correlation with
419 chlorophyll-a concentration in the surface layer (0-100m), as evidenced by a significant Spearman correlation coefficient of
420 0.65 (p-value = $9.3 \cdot 10^{-22}$, Fig. S3). In contrast, the other three morphotypes (small, bright, and aggregates, Fig. 6.A.C.D)
421 exhibited different dynamics. They were present in all three MaP features described above, whereas the elongated particles
422 did not appear to be extensively involved. The dense aggregates morphotype (purple in Fig. 5.C) is the most abundant during
423 these three features (Fig. 6.A-C).

424 2.4 Vertical distribution of particle community composition inside and outside massive export features

425 Here we analyze the distribution of the four morphotypes in the water column during the three export features (Fig. 5.D).
426 Indeed, a shift is observed in their relative proportion between the surface and the layers below. Specifically, the abundance
427 of small particles (salmon pink in Fig. 5.D) and dense aggregates (purple) increases, while the proportion of elongated and
428 bright morphotypes decreases. For example, in column 3, the proportion of small morphotypes incremented from 12% to 23%
429 and from 25% to 47% in dense aggregates. Furthermore, the distribution of morphotypes within each export feature did not
430 change considerably, except perhaps in the case of column 2.

431 2.5 The eddy dynamic context

432 The first and the second export feature occurred at the boundary between a cyclonic and an anticyclonic eddy (Fig. 1. B.C).
433 This region was therefore characterized by very intense submesoscale frontal dynamics. During the second feature (Fig. 1. C),
434 the position of the cyclone did not change significantly. The float entered the cyclone but remained close to its $R_{V_{max}}$ boundary
435 and thus within the submesoscale frontal region of the cyclone edge. Indeed, the eddy frontal regions extend over an area of
436 10-20 km across the region of eddy maximum azimuthal velocity (i.e., across $R_{V_{max}}$) as shown in Barabinot et al., (2023). This
437 second feature ended when the float was expelled from the cyclone and began to be advected southward, leaving the frontal

a supprimé: 2

a supprimé: . 7

a supprimé: . 8

441 region. The third export occurred when the float was advected around the southern edge of a large anticyclone (Fig. 1.D), again
442 a submesoscale frontal region.

a supprimé: 9

443 2.6 Impact of the three features on the upper 600m water column

444 Figure 4 clearly illustrates the high abundance of particulate carbon associated with the three export events, with their influence
445 extending down to 600 m depth. The abundance increased by a factor of 2-3 (with a factor of more than 7 during the first
446 feature) compared to periods when the Argo float was moving 'outside' these frontal regions. An average increase in MiP POC
447 of about 25% is also observed for the first and the second features. Importantly, the three features occurred during the surface
448 production period and do not show a signature in smaller particle abundances (as indicated by the absence of such a pattern in
449 fluorescence and *bbsr*, Fig. 2.D.E). In particular, MiP and MaP abundances between 100 and 1000 m were significantly
450 correlated with intense FTLE values (Spearman's rank correlation coefficient of 0.4, p-value = 4.10^{-4} and 0.49, p-value =
451 $1.3.10^{-5}$ respectively, Fig. S4-S5). Mean MiP abundance, at this depth, was also significantly correlated with low AOU values
452 (coefficient correlation of -0.59, p-value = $1.6.10^{-8}$, Fig. S6).

a supprimé: columns

a supprimé: -

a supprimé: 3

a supprimé: 4

a supprimé: 5

453 3 Discussion

454 3.1 Drivers of marine snow production in the surface layer

455 The analysis of the chlorophyll-a time series helped to characterize the seasonality of primary production in our study area. In
456 particular, from the end of October 2021 to May 2022 (spanning spring and summer), there was a significant increase in surface
457 layer chlorophyll-a concentrations (Fig. 2.D). This observation is consistent with the existing knowledge on the seasonality of
458 phytoplankton in the southern part of the Atlantic Ocean (Thomalla et al., 2011) and led us to consider this period as the
459 productive period.

460 Regarding the spatiotemporal distribution of MiP and MaP (Fig. 3.B), the abundance of MaP (i.e. aggregates) in the surface
461 layer (0-100m) was significantly correlated with the surface Lagrangian chlorophyll-a 15 days backward (see Fig. S2) and
462 high FTLE, indicating a strong biophysical coupling via several synergistic mechanisms (enhanced primary production,
463 coagulation, transport). Ocean eddies, especially cyclones, have the potential to enhance primary production by upwelling
464 nutrient-rich water from deeper layers to the surface (Benitez-Nelson et al., 2007; Ascani et al., 2013; Cornec et al., 2021).
465 This leads to the biomass accumulation at the edges of cyclones due to water mass divergence (water mass flow from the
466 center to the cyclone periphery), resulting in aggregate formation between submesoscale structures (Lima, 2002). Eddies can
467 also move phytoplankton patches through eddy stirring or trapping (McGillicuddy, 2016), leading to the accumulation of
468 organic matter at the eddy boundaries (Fig. 7.1). This implies that actively growing phytoplankton transported by the water
469 body in the previous days could have contributed to increase the abundance of MaPs by aggregation of organic matter and
470 biological activity. Among the MaP, large particles classified as elongated type were mostly found at the surface and they were
471 the best correlated with surface chlorophyll-a. Their origin is difficult to determine. Their filamentous morphology suggests a

a supprimé: Lagrangian chlorophyll

a supprimé: Cornec et al., 2021; Ascani et al., 2013;

a supprimé: 10.1

481 resemblance to chain-forming diatom colonies. The average size of particles classified under the 'elongated' morphotype is
482 approximately 820 μm ($\pm 96 \mu\text{m}$). Given their size and the study area, it's likely that some of these particles could include
483 colonies of *Chaetoceros sp.*, which are known to form filamentous structures and to dominate phytoplanktonic blooms during
484 the austral summer (Laubscher et al., 1993). They could also be Euphausiid fecal pellets, however, this kind of organisms was
485 not observed at the surface by the UVP6 which could be attributed to their potential avoidance behavior, making their
486 identification challenging. However, given their size ($>500 \mu\text{m}$), it is unlikely that they are copepod fecal pellets, most of
487 which are smaller than 200 μm (Møller et al., 2011). The other categories of MaPs are also abundant and could be the result
488 of the aggregation into larger particles by biophysical coagulation or trophic activities. Coagulation is responsible for the
489 production of large particles when both particle concentrations and stickiness are high. Additionally, a heterogeneous particle
490 size distribution enhances coagulation, as smaller particles have a higher probability of colliding with larger particles (Hunt,
491 1982; McCave, 1984; Jackson, 1990). Through this mechanism, particle encounter rates are enhanced by Brownian motion,
492 shear and/or differential settling resulting in the formation of a single, larger particle (Jackson, 1990; Stemmann et al., 2004)
493 on a timescale of a few days, as already suggested in the Southern Ocean (Jouandet et al., 2014). By affecting photosynthesis
494 and water movement, the observed intense mesoscale and submesoscale dynamics, (Fig. 1.B.C.D), could significantly affect
495 particle concentration and the probability of aggregation. The second aggregation mechanism by zooplankton grazing, sloppy
496 feeding (Lampitt et al., 1990) and fecal pellet production (Turner, 2015), occurs at long temporal scales due to the slower
497 growth time of zooplankton. Our observation strategy with a float cannot rule this aggregation mechanism out. However, it
498 seems that typical mesozooplankton fecal pellets (a few hundred μm) were not observed in abundance in, at least, three of the
499 four morphotypes. We haven't also observed a clear increase in zooplankton abundance during the three particle distribution
500 events. However, a slight increase in copepod abundance was noted during the first and third features within the first 100
501 meters (see Fig. S7). In our case, it is more likely that physical coagulation had a greater influence on aggregate formation,
502 however, we cannot rule out trophic biological aggregation. In fact, MaP were present at the surface only during the period of
503 maximum chlorophyll-a concentration and were associated with intense FTLE values (greater than 0.45 days^{-1}), which can be
504 used as a proxy of water masses convergence (i.e. frontal zones as in Prants, 2013; Hernández-Carrasco et al., 2018). In other
505 words, MaP concentrations may have been enhanced due to the combination of two important factors for coagulation according
506 to the model of Jackson (1990), increased shear associated with high hydrodynamics at front and enhanced phytoplankton
507 biomass.

a supprimé: Their origin is difficult to assess, but their filamentous morphology makes them resemble chain-forming diatoms or other phytoplankton colonies.

a supprimé: Coagulation is responsible for the production of large particles when particle concentrations become important in the water column (Jackson et al. 1990)

a supprimé: s. 7-9

a supprimé: However, typical mesozooplankton fecal pellets (a few hundred μm) were not observed in abundance in any of the four morphological categories. We haven't also observed a zooplankton abundance increase during the three particle distribution events (see Figure S6). In our case, it is more likely that physical coagulation had a greater influence on aggregate formation than trophic biological aggregation.

a supprimé: (i.e. frontal zones). In other words, they could benefit from a combination of high hydrodynamic and strong phytoplankton production, consistent with the model analysis proposed by Jackson (1990) for coagulation.

508 3.2 Coupling between massive export of large aggregates and regional ocean dynamics

509 Analysis of the spatio-temporal distribution of particles has revealed three regions of enhanced concentration of particles at
510 depth, suggesting that vertical export of organic matter occurred in these areas during the productive season. These were
511 characterized by intense MaP and MiP abundances extending vertically from the surface to depths of about 600 m. These
512 export regions were associated with high FTLE values suggesting frontogenesis-driven mechanisms during which there could
513 be a strong coupling between gravitational sinking of particles and intensified physical vertical velocities.

532 3.2.1 A submesoscale frontogenesis-driven mechanism

533 The abundance of particles such as MaP and MiP below the MLD (100-600m) was positively correlated with the surface
534 Lagrangian FTLE as well as for the small, bright and aggregated morphotypes. Large FTLE values can identify convergence
535 of water masses with different hydrological properties, creating intense density gradients. It is known that intense velocity and
536 density gradients arise in correspondence with mesoscale (geostrophic) and submesoscale (ageostrophic) frontogenesis, e.g. at
537 the edge of mesoscale features (Freilich and Mahadevan, 2021). At such fronts upper-ocean waters converge and subduct
538 beneath the mixed layer into the stratified pycnocline (e.g. Omand et al. 2015) or also in deeper layers (e.g. Llort et al., 2018).
539 These regions are typically associated with significant vertical velocities (up to 20 m/day). Frontal patterns, in the potential
540 density time series, are clearly seen extending into the ocean interior (Fig. 2.C) and are also found to correspond to the three
541 intense export features. During these features, the signal reached about 1000 m. All of them were located at the periphery of
542 mesoscale eddies (Fig. 1. B.C.D), where the vertical velocity is expected to be higher (Thomas et al., 2008; Freilich and
543 Mahadevan, 2019). Unfortunately, it was not possible to calculate vertical velocities from the data provided by the BGC Argo
544 profiler.

545 Previous studies in a similar mesoscale physical context have shown that mesoscale activity can result in the intrusion of small
546 POM-rich water masses into the mesopelagic layers (Omand et al., 2015; Llort et al., 2018). In our study, the three features
547 described, occurred from the MLD to a depth of about 600 m or deeper (i.e. over a large part of the water column), whereas
548 the subduction described in Llort et al. (2018) occurred well below the MLD in the mesopelagic in depth layers thickness of
549 about 50-100 m. We applied the Llort et al. (2018) algorithm to identify ESP events across all profiles. Only 28 profiles were
550 classified as ESP events (see Figure 1.A, yellow dots). Of these, seven were located near export features described in this
551 study. However, increases in *bbsr*, chlorophyll-a, MiP, and MaP were not consistently observed across these ESP events.
552 Furthermore, the ESP events were generally less than 100 meters thick, whereas the export features we identified extended
553 through much of the water column. These findings suggest that while some export features may be linked to ESP events, the
554 ESP alone does not appear to be a fundamental trigger for these features. This suggests that we are describing a slightly
555 different mechanism compared to Omand et al. (2015) and Llort et al. (2018) responsible for the accumulation of organic
556 matter at depth, but also one related to mesoscale and submesoscale processes. This highlights the fact that the influence of
557 these physical mechanisms is a challenging area of research.

558 3.2.2 The key role of the gravitational carbon pump and the MLD

559 Historically, particle size has been considered as the primary factor influencing settling velocity (Guidi et al., 2008). However,
560 with advances in imaging systems, it has become increasingly clear that particle morphology has a significant effect on settling
561 velocities (Iversen and Lampitt, 2020; Cael et al., 2021; Williams and Giering, 2022). This process supports the idea that larger
562 (large ESD, size characteristic) and more compact (non-porous, morphological property) particles will sink faster. In this study,
563 direct estimates of settling particle velocity (e.g. export plume methodology; Stemmann et al., 2002; Briggs et al., 2020;

a supprimé: Figs. 7-9

a supprimé: 2

566 Trudnowska et al., 2021) could not be computed due to the non-completely Lagrangian nature of the float. However, it is
567 possible to assume that the morphotypes identified in this work have different sinking velocities with the highest for
568 small/dense and dark aggregate morphotypes (which dominate in the deepest water column, Fig. 5.D) and the lowest for the
569 elongated morphotypes because they are only found at the surface (Fig. 5.B). In addition, the particles with the higher
570 velocities should be rapidly exported to depth, so they should spend less time in the upper water column than particles with
571 the lowest sinking velocity. In other words, the latter will be more exposed to remineralization.

572 Furthermore, the analysis of the morphotype distribution during the three export features showed a shift in the group
573 proportions between the surface layer (0-100m, which is approximately the mean depth of the MLD, all profiles included) and
574 deeper layers (100-1000m). This shift favored small and dense aggregate groups (in terms of proportion) between these two
575 layers. **These morphotypes probably have the highest sinking speed (Soviadan et al., 2024).** This supports the idea that the
576 MLD could act as a physical barrier (Hosoda et al., 2010) and only sinking particles were able to cross it. This conclusion is
577 also supported by the fact that, in most profiles, only MiP and especially MaP are located below the MLD, while small labile
578 and refractory particles (*bbsr*) and chlorophyll-containing particles were rarely found below the MLD. Among the MaP, the
579 sinking explanation is valid for three morphotypes (small particles, bright and dense aggregates), but not for the elongated
580 types that we hypothesized to **be chain-forming diatom colonies (*Chaetoceros sp.*)**. This result further emphasizes the critical
581 importance of considering morphology and not just particle size when analyzing the size of particles in marine snow dynamics
582 and when calculating vertical fluxes using only allometric relationships.

583 Another result is that features 1 and 3 show minimal changes in morphotype proportions between layer depths. In fact, it would
584 be expected that the relative proportion of each morphotype would vary with depth due to their presumed different settling
585 rates. It is possible that the morphotypes do not have different settling rates and settle at similar rates. Alternatively, there may
586 be some other mechanism at work that is significantly more important than settling velocity and is responsible for transporting
587 particles to deeper regions, which will be discussed below.

588 3.2.3 Possible coupling with vertical velocities

589 During the three described features, MiP abundance between 100 and 1000 meters was significantly correlated with low AOU
590 values. AOU is a proxy for the age of water masses (Sarmiento, 2006), with lower AOU values indicating that the water masses
591 had a more recent contact with the surface. The significant negative correlation between AOU and 100-1000 m MiP abundance
592 suggests a physical downward transport leading to the formation of these features. In addition, we know from the eddy
593 detection algorithm that each export feature was detected in the frontal region separating two adjacent eddies of opposite
594 polarity. Mesoscale activity is known to play an important role in the vertical distribution of water masses.

595 In addition, surface frontal regions develop ageostrophic secondary circulations (Lévy et al., 2018) that lead to intense vertical
596 velocities, which can be stronger at the edges of cyclonic structures and can be on the order of 100 m d⁻¹ or more (Mahadevan

a supprimé: These morphotypes should have the highest sinking rate.

a supprimé: be large phytoplankton

a supprimé: C

a supprimé: (Capó et al., 2021; Freilich & Mahadevan, 2021; Tarry et al., 2021; Siegelman et al., 2020; Mahadevan et al., 2016; McWilliams, 2016;

604 & Archer, 2000; Mahadevan et al., 2016; McWilliams, 2016; Freilich & Mahadevan, 2019; Siegelman et al., 2020; Capó et
605 al., 2021; Tarry et al., 2021). This is further supported by several studies that show that the presence of mesoscale eddies
606 greatly enhances the vertical transport of water properties (Omand et al., 2015, Llorc et al., 2018, Couespel et al., 2024). In the
607 study region, mesoscale ocean dynamics are particularly active, with eddies generated by the Agulhas Current (the Agulhas
608 rings), the Agulhas Bank (the Agulhas lee cyclones), the Benguela upwelling, and subantarctic front cyclones. All can influence
609 the water column to depths of up to 1600 meters (Schmid et al., 2003). While these dynamics are known to exist, their impact
610 on the vertical exchange of properties through the water column remains to be assessed. However, a recent study (Siegelman
611 et al., 2020) has shown that such vertical velocities are enhanced below the MLD, which acts as a buffer for them, by relatively
612 deep submesoscale fronts. This result may explain why only large particles (i.e., MiP, MaP, and morphotypes) involved in the
613 gravitational pump and capable of crossing the physical barrier represented by the MLD are entrained in this process. However,
614 we lack information on the 3D context of the water mass, both in terms of currents and biogeochemical properties, which
615 makes it impossible to determine what happened at depth before the float passed. Consequently, it's impossible to rule out the
616 action of lateral advection on the mechanism described in this study. Nevertheless, the strong correlation between the described
617 events, the FTLE, and the positions of the eddies suggests a significant link to vertical rather than lateral advection. In addition,
618 previous studies have shown that frontal structures identified by Lyapunov Exponents ridges at the surface can persist in the
619 water column (Bettencourt et al., 2012), corroborating our findings. The hypothesis that the gravitational pump may be
620 associated with physical processes related to mesoscale activity has already been proposed by Guidi et al. (2007). The authors
621 found that the natural gravitational settling of particles combined with the associated vertical velocities of the water masses
622 triggered the export of particles into the deep Atlantic. Such a physical mechanism associated with the gravitational pump
623 would be a key process of carbon export to the deep ocean observed in our study.

624 4 Conclusion

625 As described in the conceptual schematic (Fig. 7), mesoscale frontal dynamics between cyclones and anticyclones seem to
626 have a profound effect on particle distribution down to 600 m depth. We propose that particle concentration at these locations
627 is enhanced by increased primary production and/or horizontal convergence induced by frontal activity or trapping. As a result,
628 coagulation processes may have been enhanced, with the ultimate result being the formation of larger aggregates. These
629 particles could have sunk below the MLD, in particular the large and/or dense ones, due to their higher sinking velocities. The
630 consistently observed vertical distribution of particles from the surface to a depth of 600 m suggests that their downward
631 transport is extremely rapid. We propose that such features result from the combination of the relatively large sinking speed
632 of such particles (likely due to their great density), and the enhanced vertical motion of the water induced by submesoscale
633 frontal dynamics, in particular below the MLD. If such a phenomenon is influenced by deeper mesoscale structures, it is likely
634 to extend into deeper layers. Such vertical transport is an integral part of the physical particle injection pump, particularly a
635 unique frontal subduction pump, characterized by intense vertical velocities that might materialize in intense frontal regions.

a supprimé: 10

a supprimé: turbulence

a supprimé: a coupling between their own sedimentation rate
(the gravitational carbon pump)

640 However, the relatively coarse temporal resolution of our dataset did not enable us to calculate the according vertical velocities,
641 and we hence could not disentangle the gravitational and subduction pump in more detail.

642 Our study suggests that small-scale ocean dynamics represent an efficient particle injection pump that can enhance the
643 efficiency of the biological pump by increasing the depth of carbon transport. It is crucial to note that the explicit mechanisms
644 underlying these features are not fully defined due to the temporal and spatial limitations imposed by the Argo float's lack of
645 resolution. Additionally, the submesoscale nature of these features introduces high variability in both space and time. This
646 study underscores the significance of implementing repeated sampling campaigns or the use of gliders equipped with UVP6
647 and further sensors (e.g. microstructure) and focusing on the interface zones between eddies. Such studies would help to
648 validate our proposed mechanism, and to disentangle the relative contribution of the various PIPs processes (such as ESP). In
649 particular, focus on such studies needs to be put on resolving the water movements (e.g. the vertical velocities) to enable the
650 separation of the passive sinking and vertical translocation of particles. Since mesoscale and submesoscale structures are
651 ubiquitous in the ocean, it would also be interesting to quantify the influence of this type of process on the overall carbon
652 budget and to determine the extent to which it contributes to carbon sequestration in the deep ocean, information that is crucial
653 in the context of global change.

a supprimé: s

a supprimé: and would improve our understanding of the mechanisms involved in this process. Since mesoscale and submesoscale structures are ubiquitous in the ocean, it would also be interesting to quantify the influence of this type of process on the overall carbon budget

654 5 Author contribution

655 A.A., R.K.: SS and L.S.: designed the study

656 A.A.: conducted data analysis, interpreted results, drafted the manuscript, under guidance of RK and LS

657 AB and RL.: supported the study by environmental background data analysis, revised manuscript.

658 R.K. and S.S.: contributed to the conception of the study, revised manuscript.

659 R.K.: coordinated the recapture of the float

660 L.S.: contributed to the conception and design of the study, supervised the analysis, substantively revised the manuscript.

661 6 Competing interests

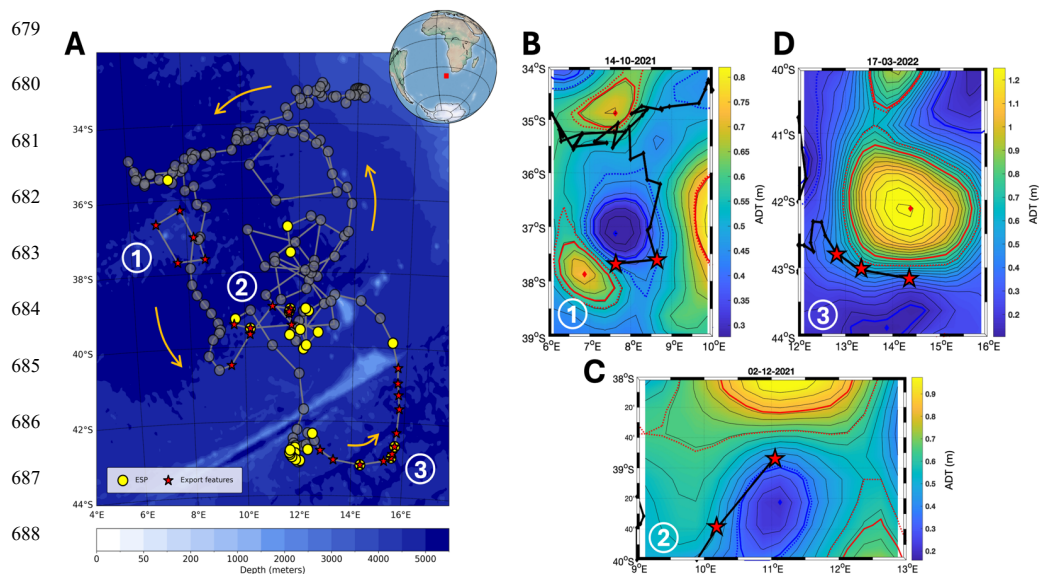
662 The authors declare that they have no conflict of interest.

663 7 Acknowledgments

664 This study would not have been possible without the support of the crews of the Research Vessel Sonne from Germany and
665 the SA Agulhas II from South Africa. We acknowledge the work of Marc Picheral, Edouard Laymarie, Antoine Poteau and
666 Camille Catalano from the Laboratory of Villefranche sur Mer in helping with the UVP6 logistic and quality control. We also
667 thank the Quantitative Imaging Platform of Villefranche-sur-Mer (PIQv) for providing us with their taxonomic expertise. This

674 work was supported by the TRIATLAS project, which has received funding from the European Union's Horizon 2020 research
675 and innovation program under grant agreement No 817578. RK furthermore acknowledges support via a Make Our Planet
676 Great Again grant from the French National Research Agency (ANR) within the Programme d'Investissements d'Avenir ANR-
677 19-MPGA-0012 and funding from the Heisenberg Programme of the German Science Foundation KI 1387/5-1.

678 **Figures**



690 **Figure 1: (A) Float trajectory (thick gray line) during its entire deployment from April 2021 to September 2022 in the South-East**
691 **Atlantic Ocean. Orange arrows indicate the direction of the float trajectory. Stars highlight export features described in our study**
692 **(1 to 3 in panels B, C and D). Yellow dots indicate Eddy Subduction Pump (ESP) events (defined as in Llorc et al., 2018). Shaded**
693 **gray dots indicate profiles during which no export features were detected. The background map is the bathymetry of the study zone.**
694 **(B), (C) and (D) panels show ADT field snapshots with the float trajectory (thick black line) during each export feature. Cyclones**
695 **and anticyclones are associated with blue and red colors, respectively. Diamonds show eddies centroid. Thick solid lines correspond**
696 **to eddies maximum speed. Thin solid lines correspond to ADT isolines. Dashed lines to eddies outer limit definition.**

a supprimé: Figure 1: Float trajectory (thick black line) with profiles realized (185; black dots) during its deployment from April 2021 to September 2022. The map background is a snapshot of the ADT field in September 2022 showcasing the intense mesoscale activity of the study zone.

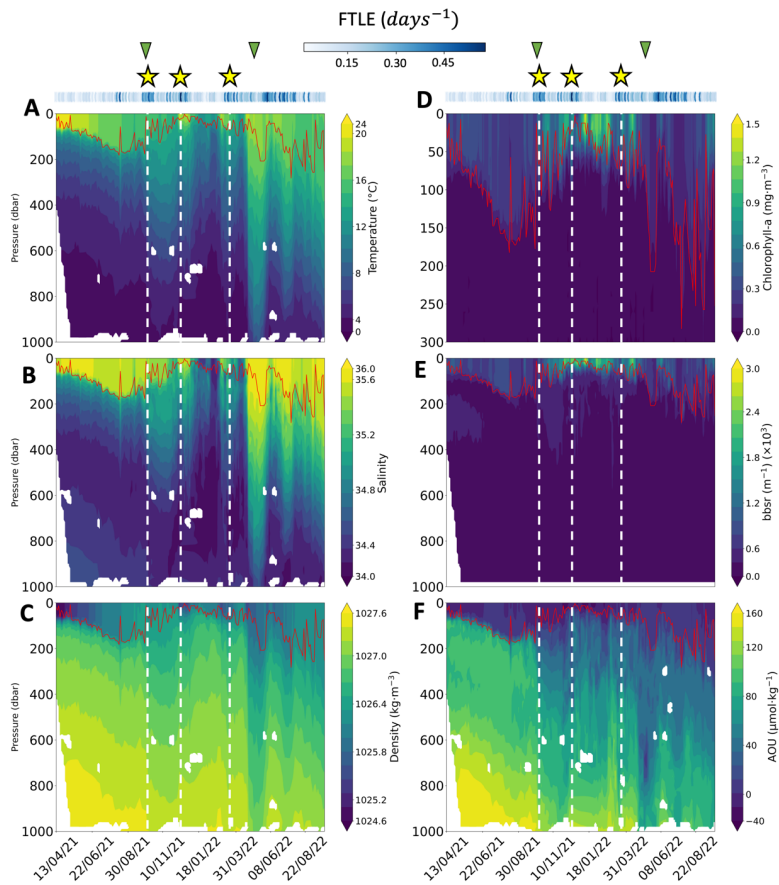


Figure 2: Hydrographic and biogeochemical properties as a function of time and depth along the float trajectory (1.5 years, from April 2021 to September 2022). The panels show (A) temperature, (B) salinity, (C) potential density, (D) chlorophyll-a concentration, (E) \log_{10} of 700 nm optical backscatter bbsr, (F) Apparent Oxygen Utilization (AOU). The red solid line in each panel shows the mixed layer depth (MLD). The white dashed lines and the yellow stars show the location of intense exports of particles. The green triangles indicate the start and the end of the production period. Blue dots on top of the panel show the mean five days backward FTLE (days^{-1}) for each profile location.

a supprimé: ¶

a supprimé: ¶

731
732
733
734
735
736
737
738
739
740
741
742
743
744
745
746
747
748
749
750
751
752
753
754
755
756
757
758

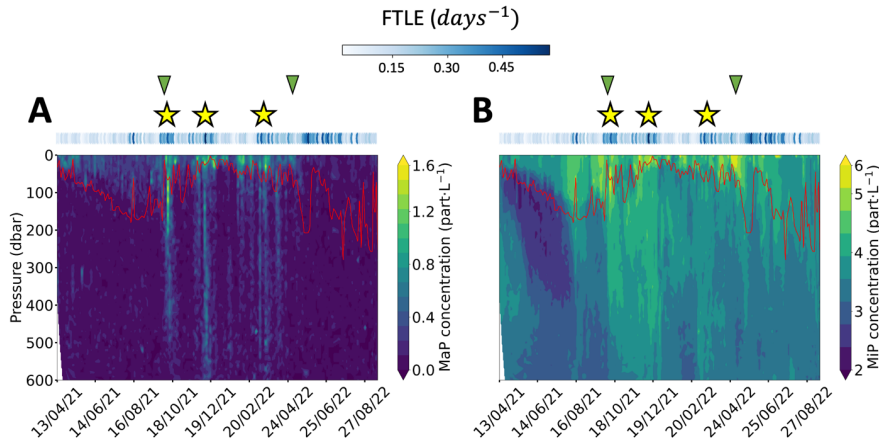


Figure 3: Particles spatio-temporal distribution. The panels show, (A) MiP (Micrometric Particles $0.1 < \text{ESD} < 0.5 \text{ mm}$) concentrations, (B) MaP (Macrometric Particles $0.6 < \text{ESD} < 16 \text{ mm}$) concentrations. Both concentrations were log transformed. Red solid line represents the MLD. Yellow stars show the location of intense exports of particles. Green triangles give the start and the end of the production period. Blue dots on top of the panels show five days backward FTLE (days^{-1}) for each profile location.

759
760
761
762
763
764
765
766
767
768
769
770
771
772
773
774
775
776
777
778
779
780
781
782
783

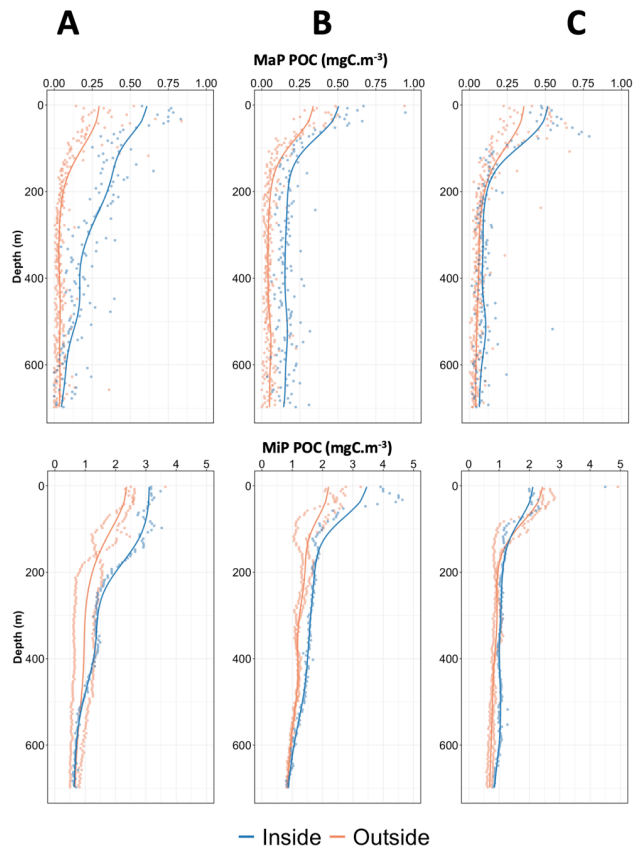


Figure 4: Comparison of MiP POC (top panels) and MaP POC (bottom panels) in the water column both outside and inside each export feature. The panels show, (A) the first export feature (01-10-2021 – 17/10/2021), (B) the second one (01-12-2021 – 19-12-2021) and (C) the last one (01/03/2022 – 28/03/2022). The dots on the graph represent the data averaged over 5-meter bins. The solid lines are a moving average of the 5-meter bins data. The orange signal corresponds to the average of profiles recorded one month prior to and after each feature (outside), while the blue signal corresponds to the average profiles recorded during each feature (inside).

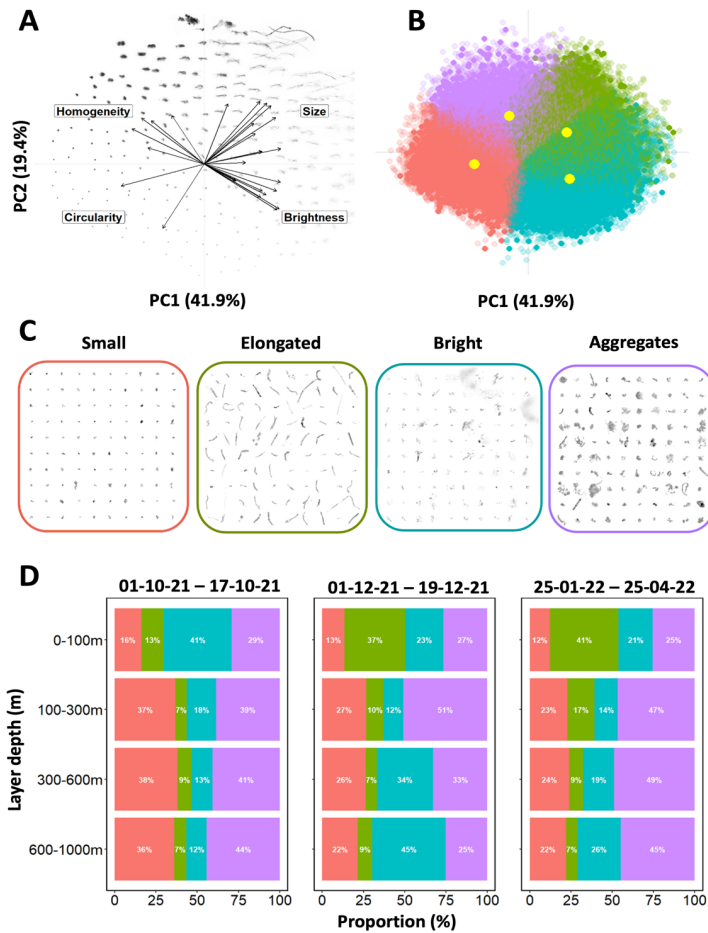


Figure 5: Results of PCA/K-means clustering on morphological traits of particles. Panels show, (A) the distribution of particle images in the morphospace built by PCA, (B) the K-means clustering classification where each point represents an image, and each cluster is colored independently. The yellow dots represent the center of each cluster. The most transparent dots represent images not retained in the analysis, (C) Representative subset of each morphotype and (D) the proportion (%) of each group according to depth layers during the three export features observed in the morphotypes spatio-temporal distribution. The color code is the same for (B), (C) and (D).

809
810
811
812
813
814
815
816
817
818
819
820
821
822
823
824
825
826
827
828
829
830
831
832
833
834
835
836
837
838
839
840
841
842
843
844
845
846

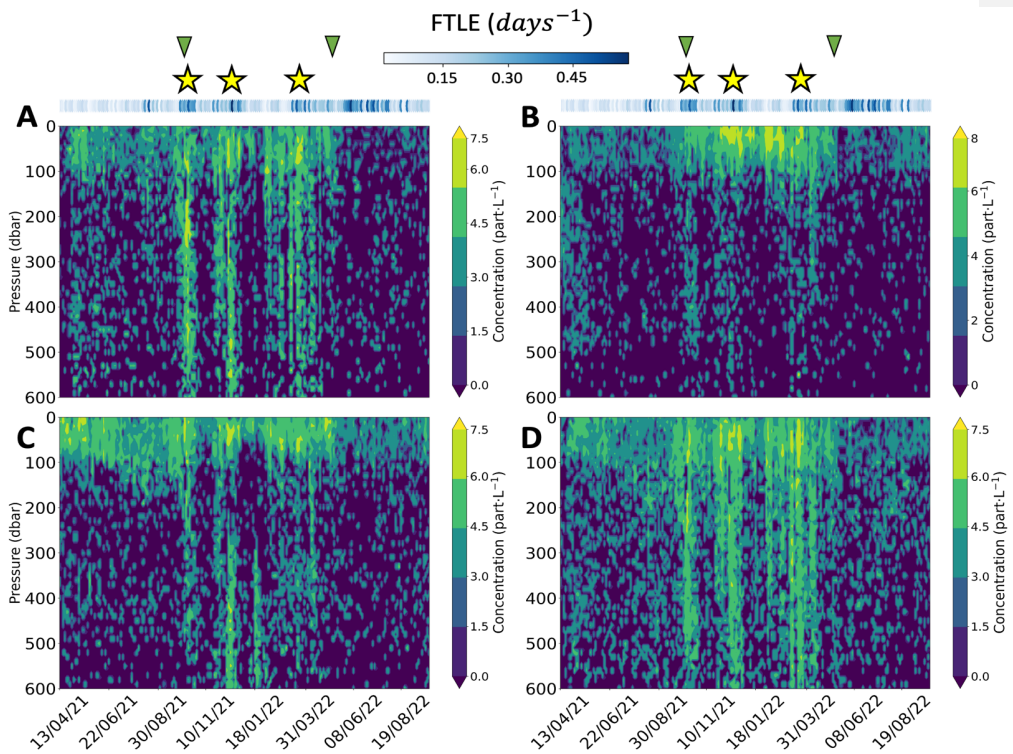


Figure 6: Morphotypes spatio-temporal distribution of exclusive members. The panels show log transformed concentrations ($part.L^{-1}$) of (A) Small, (B) Elongated, (C) Bright and (D) Aggregates morphotypes. Yellow stars and green triangles have the same meaning as in the Figure 2

a supprimé: White dashed lines, y

848
849
850
851
852
853
854
855
856
857
858
859
860
861
862
863
864
865
866
867
868
869
870
871
872
873
874
875
876
877
878
879
880
881
882
883
884
885

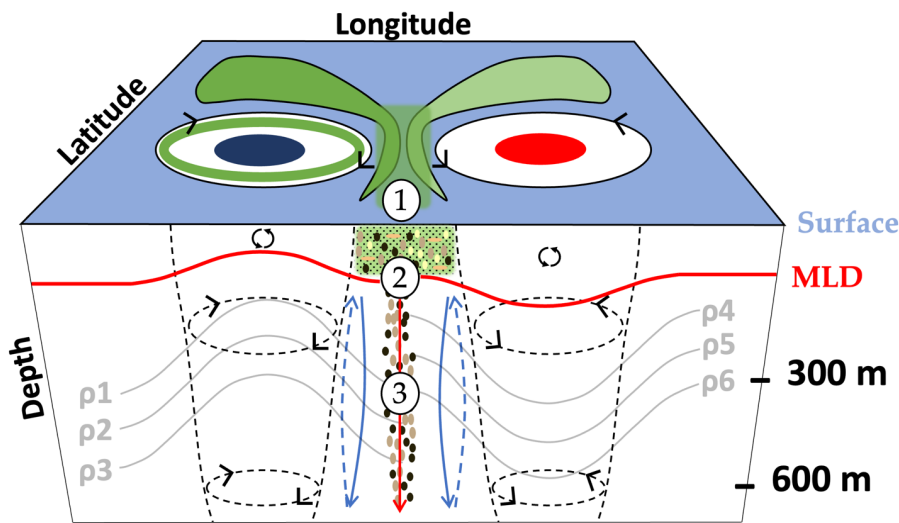


Figure 7: Schematic view of the proposed mechanism for the deep observed accumulation of particulate carbon in the mesoscale context of the study. (1) Aggregation and coagulation of surface organic matter (green shapes around eddies), facilitated by eddy trapping or stirring. The green circle in the cyclone represents the accumulation of POM at its periphery (resulting from the divergence of the water masses) (2) Influence of the Gravitational Carbon Pump (represented by the red vertical arrow) that transporting selected marine snow types with sufficient downward speed beneath the Mixed Layer Depth (MLD). (3) Coupling with a frontogenesis mechanism inducing enhanced physical vertical speeds (represented by blue arrows), particularly below the MLD and in interface zones between mesoscale structures. The coupling between (1), (2) and (3) can lead to the transport of particles down to significant depths (600 meters in our study). Black arrows in the MLD represent the physical mixing.

a supprimé: <object>

Figure 7: Snapshot of ADT field with the float trajectory (thick black line) during each export feature (A, B and C). Cyclones and anticyclones are associated with blue and red colors, respectively. Diamonds show eddy centres.

a mis en forme : Justifié, Interligne : 1,5 ligne

a supprimé: Figure 8: Schematic view of the proposed mechanism for the deep observed accumulation of particulate carbon in the mesoscale context of the study. (1) Aggregation and coagulation of surface organic matter, facilitated by eddy trapping or stirring. (2) Influence of the Gravitational Carbon Pump (represented by the red vertical arrow) that transporting particles with sufficient downward speed beneath the Mixed Layer Depth (MLD). (3) Coupling with a frontogenesis mechanism inducing enhanced physical vertical speeds (represented by blue arrows), particularly below the MLD and in interface zones between mesoscale structures. The coupling between (1), (2) and (3) can lead to the transport of particles down to significant depths (600 meters in our study). Black arrows in the MLD represent the physical mixing.

980 **References**

- 981 Alldredge, A.: The carbon, nitrogen and mass content of marine snow as a function of aggregate size, *Deep Sea Research Part*
982 *I: Oceanographic Research Papers*, 45, 529–541, [https://doi.org/10.1016/S0967-0637\(97\)00048-4](https://doi.org/10.1016/S0967-0637(97)00048-4), 1998.
- 983 Alldredge, A. L. and Gotschalk, C.: In situ settling behavior of marine snow1: Sinking rates of marine snow, *Limnol.*
984 *Oceanogr.*, 33, 339–351, <https://doi.org/10.4319/lo.1988.33.3.0339>, 1988.
- 985 Ascani, F., Richards, K. J., Firing, E., Grant, S., Johnson, K. S., Jia, Y., Lukas, R., and Karl, D. M.: Physical and biological
986 controls of nitrate concentrations in the upper subtropical North Pacific Ocean, *Deep Sea Research Part II: Topical Studies in*
987 *Oceanography*, 93, 119–134, <https://doi.org/10.1016/j.dsr2.2013.01.034>, 2013.
- 988 Azetsu-Scott, K. and Johnson, B. D.: Measuring physical characteristics of particles: a new method of simultaneous
989 measurement for size, settling velocity and density of constituent matter, *Deep Sea Research Part A. Oceanographic Research*
990 *Papers*, 39, 1057–1066, [https://doi.org/10.1016/0198-0149\(92\)90039-V](https://doi.org/10.1016/0198-0149(92)90039-V), 1992.
- 991 Ballarotta, M., Ubelmann, C., Pujol, M.-I., Taburet, G., Fournier, F., Legeais, J.-F., Faugère, Y., Delepouille, A., Chelton, D.,
992 Dibarboue, G., and Picot, N.: On the resolutions of ocean altimetry maps, *Ocean Sci.*, 15, 1091–1109,
993 <https://doi.org/10.5194/os-15-1091-2019>, 2019.
- 994 Barabinot, Y., Speich, S., and Carton, X. J.: Defining Mesoscale Eddies Boundaries from In-situ Data and a Theoretical
995 Framework, Preprints, <https://doi.org/10.22541/essoar.167870447.76933252/v1>, 2023.
- 996 Baudena, A., Ser-Giacomi, E., D’Onofrio, D., Capet, X., Cotté, C., Cherel, Y., and D’Ovidio, F.: Fine-scale structures as spots
997 of increased fish concentration in the open ocean, *Sci Rep*, 11, 15805, <https://doi.org/10.1038/s41598-021-94368-1>, 2021.
- 998 Baudena, A., Laxenaire, R., Catalano, C., Claustre, H., Ioannou, A., Leymarie, E., Picheral, M., Poteau, A., Speich, S.,
999 Stemmann, L., and Kiko, R.: A Lagrangian perspective on the carbon and oxygen budget of an oceanic eddy, preprint,
1000 <https://doi.org/10.21203/rs.3.rs-3014931/v1>, 2023.
- 1001 Benitez-Nelson, C. R., Bidigare, R. R., Dickey, T. D., Landry, M. R., Leonard, C. L., Brown, S. L., Nencioli, F., Rii, Y. M.,
1002 Maiti, K., Becker, J. W., Bibby, T. S., Black, W., Cai, W.-J., Carlson, C. A., Chen, F., Kuwahara, V. S., Mahaffey, C.,
1003 McAndrew, P. M., Quay, P. D., Rappé, M. S., Selph, K. E., Simmons, M. P., and Yang, E. J.: Mesoscale Eddies Drive Increased
1004 Silica Export in the Subtropical Pacific Ocean, *Science*, 316, 1017–1021, <https://doi.org/10.1126/science.1136221>, 2007.
- 1005 Benson, B. B. and Krause, D.: The concentration and isotopic fractionation of oxygen dissolved in freshwater and seawater in
1006 equilibrium with the atmosphere1: Oxygen solubility in seawater, *Limnol. Oceanogr.*, 29, 620–632,
1007 <https://doi.org/10.4319/lo.1984.29.3.0620>, 1984.

1008 Bettencourt, J. H., López, C., and Hernández-García, E.: Oceanic three-dimensional Lagrangian coherent structures: A study
1009 of a mesoscale eddy in the Benguela upwelling region, *Ocean Modelling*, 51, 73–83,
1010 <https://doi.org/10.1016/j.ocemod.2012.04.004>, 2012.

1011 Bisson, K., Siegel, D. A., and DeVries, T.: Diagnosing Mechanisms of Ocean Carbon Export in a Satellite-Based Food Web
1012 Model, *Front. Mar. Sci.*, 7, 505, <https://doi.org/10.3389/fmars.2020.00505>, 2020.

1013 [Boebel, O., Lutjeharms, J., Schmid, C., Zenk, W., Rossby, T., and Barron, C.: The Cape Cauldron: a regime of turbulent inter-
1014 ocean exchange. *Deep Sea Research Part II: Topical Studies in Oceanography*, 50, 57–86, \[https://doi.org/10.1016/S0967-
1015 0645\\(02\\)00379-X\]\(https://doi.org/10.1016/S0967-

1015 0645\(02\)00379-X\), 2003.](https://doi.org/10.1016/S0967-0645(02)00379-X)

1016 Boyd, P. W., Claustre, H., Levy, M., Siegel, D. A., and Weber, T.: Multi-faceted particle pumps drive carbon sequestration in
1017 the ocean, *Nature*, 568, 327–335, <https://doi.org/10.1038/s41586-019-1098-2>, 2019.

1018 Briggs, N., Dall’Olmo, G., and Claustre, H.: Major role of particle fragmentation in regulating biological sequestration of CO
1019 ₂ by the oceans, *Science*, 367, 791–793, <https://doi.org/10.1126/science.aay1790>, 2020.

1020 Cael, B. B., Cavan, E. L., and Britten, G. L.: Reconciling the Size-Dependence of Marine Particle Sinking Speed, *Geophysical
1021 Research Letters*, 48, <https://doi.org/10.1029/2020GL091771>, 2021.

1022 Capó, E., McWilliams, J. C., Mason, E., and Orfila, A.: Intermittent Frontogenesis in the Alboran Sea, *Journal of Physical
1023 Oceanography*, 51, 1417–1439, <https://doi.org/10.1175/JPO-D-20-0277.1>, 2021.

1024 Chaigneau, A., Eldin, G., and Dewitte, B.: Eddy activity in the four major upwelling systems from satellite altimetry (1992–
1025 2007), *Progress in Oceanography*, 83, 117–123, <https://doi.org/10.1016/j.pocean.2009.07.012>, 2009.

1026 [Chaigneau, A., Le Texier, M., Eldin, G., Grados, C., and Pizarro, O.: Vertical structure of mesoscale eddies in the eastern
1027 South Pacific Ocean: A composite analysis from altimetry and Argo profiling floats, *J. Geophys. Res.*, 116, 2011JC007134,
1028 <https://doi.org/10.1029/2011JC007134>, 2011.](https://doi.org/10.1029/2011JC007134)

1029 Chambault, P., Baudena, A., Bjorndal, K. A., Santos, M. A. R., Bolten, A. B., and Vandeperre, F.: Swirling in the ocean:
1030 Immature loggerhead turtles seasonally target old anticyclonic eddies at the fringe of the North Atlantic gyre, *Progress in
1031 Oceanography*, 175, 345–358, <https://doi.org/10.1016/j.pocean.2019.05.005>, 2019.

1032 Cornec, M., Laxenaire, R., Speich, S., and Claustre, H.: Impact of Mesoscale Eddies on Deep Chlorophyll Maxima,
1033 *Geophysical Research Letters*, 48, e2021GL093470, <https://doi.org/10.1029/2021GL093470>, 2021.

1034 Couespel, D., Lévy, M., and Bopp, L.: Stronger oceanic CO₂ sink in eddy-resolving simulations of global warming,
1035 *Geophysical Research Letters*, <https://hal.science/hal-04396517/>, 2024.

a mis en forme : Anglais (E.U.)

a mis en forme : Anglais (E.U.)

Code de champ modifié

a mis en forme : Anglais (E.U.)

a mis en forme : Anglais (E.U.)

a mis en forme : Anglais (E.U.)

a mis en forme : Anglais (E.U.)

Code de champ modifié

- 1036 d'Ovidio, F., De Monte, S., Alvain, S., Dandonneau, Y., and Lévy, M.: Fluid dynamical niches of phytoplankton types, Proc.
 1037 Natl. Acad. Sci. U.S.A., 107, 18366–18370, <https://doi.org/10.1073/pnas.1004620107>, 2010.
- 1038 De Boyer Montégut, C., Madec, G., Fischer, A. S., Lazar, A., and Iudicone, D.: Mixed layer depth over the global ocean: An
 1039 examination of profile data and a profile-based climatology, J. Geophys. Res., 109, 2004JC002378,
 1040 <https://doi.org/10.1029/2004JC002378>, 2004.
- 1041 Duncombe Rae, C. M.: Agulhas retroflection rings in the South Atlantic Ocean: an overview, South African Journal of Marine
 1042 Science, 11, 327–344, <https://doi.org/10.2989/025776191784287574>, 1991.
- 1043 Dunne, J. P., Armstrong, R. A., Gnanadesikan, A., and Sarmiento, J. L.: Empirical and mechanistic models for the particle
 1044 export ratio, Global Biogeochemical Cycles, 19, 2004GB002390, <https://doi.org/10.1029/2004GB002390>, 2005.
- 1045 Fabri-Ruiz, S., Baudena, A., Moullec, F., Lombard, F., Irisson, J.-O., and Pedrotti, M. L.: Mistaking plastic for zooplankton:
 1046 Risk assessment of plastic ingestion in the Mediterranean sea, Science of The Total Environment, 856, 159011,
 1047 <https://doi.org/10.1016/j.scitotenv.2022.159011>, 2023.
- 1048 Flament, P.: A state variable for characterizing water masses and their diffusive stability: spiciness, Progress in Oceanography,
 1049 54, 493–501, [https://doi.org/10.1016/S0079-6611\(02\)00065-4](https://doi.org/10.1016/S0079-6611(02)00065-4), 2002.
- 1050 Freilich, M. A. and Mahadevan, A.: Decomposition of Vertical Velocity for Nutrient Transport in the Upper Ocean, Journal
 1051 of Physical Oceanography, 49, 1561–1575, <https://doi.org/10.1175/JPO-D-19-0002.1>, 2019.
- 1052 Garcia, H. E. and Gordon, L. I.: Oxygen solubility in seawater: Better fitting equations, Limnol. Oceanogr., 37, 1307–1312,
 1053 <https://doi.org/10.4319/lo.1992.37.6.1307>, 1992.
- 1054 [Giulivi, C. F. and Gordon, A. L.: Isopycnal displacements within the Cape Basin thermocline as revealed by the Hydrographic](#)
 1055 [Data Archive, Deep Sea Research Part I: Oceanographic Research Papers, 53, 1285–1300,](#)
 1056 <https://doi.org/10.1016/j.dsr.2006.05.011>, 2006.
- 1057 [Gorsky, G., Prieur, L., Taupier-Letage, I., Stemann, L., and Picheral, M.: Large particulate matter in the Western](#)
 1058 [Mediterranean, Journal of Marine Systems, 33–34, 289–311, https://doi.org/10.1016/S0924-7963\(02\)00063-5, 2002.](#)
- 1059 Guidi, L., Stemann, L., Legendre, L., Picheral, M., Prieur, L., and Gorsky, G.: Vertical distribution of aggregates (>110 µm)
 1060 and mesoscale activity in the northeastern Atlantic: Effects on the deep vertical export of surface carbon, Limnol. Oceanogr.,
 1061 52, 7–18, <https://doi.org/10.4319/lo.2007.52.1.0007>, 2007.
- 1062 Guidi, L., Jackson, G. A., Stemann, L., Miquel, J. C., Picheral, M., and Gorsky, G.: Relationship between particle size
 1063 distribution and flux in the mesopelagic zone, Deep Sea Research Part I: Oceanographic Research Papers, 55, 1364–1374,
 1064 <https://doi.org/10.1016/j.dsr.2008.05.014>, 2008.

a mis en forme : Anglais (E.U.)

a mis en forme : Anglais (E.U.)

a mis en forme : Anglais (E.U.)

Code de champ modifié

a mis en forme : Anglais (E.U.)

a mis en forme : Anglais (E.U.)

Code de champ modifié

- 1065 Guidi, L., Calil, P. H. R., Duhamel, S., Björkman, K. M., Doney, S. C., Jackson, G. A., Li, B., Church, M. J., Tozzi, S., Kolber,
1066 Z. S., Richards, K. J., Fong, A. A., Letelier, R. M., Gorsky, G., Stemmann, L., and Karl, D. M.: Does eddy-eddy interaction
1067 control surface phytoplankton distribution and carbon export in the North Pacific Subtropical Gyre?, *J. Geophys. Res.*, 117,
1068 2012JG001984, <https://doi.org/10.1029/2012JG001984>, 2012.
- 1069 Haller, G.: Lagrangian Coherent Structures, *Annu. Rev. Fluid Mech.*, 47, 137–162, <https://doi.org/10.1146/annurev-fluid-010313-141322>, 2015.
- 1071 Henson, S. A., Sanders, R., and Madsen, E.: Global patterns in efficiency of particulate organic carbon export and transfer to
1072 the deep ocean, *Global Biogeochemical Cycles*, 26, 2011GB004099, <https://doi.org/10.1029/2011GB004099>, 2012.
- 1073 Hernández-Carrasco, I., Orfila, A., Rossi, V., and Garçon, V.: Effect of small scale transport processes on phytoplankton
1074 distribution in coastal seas, *Sci Rep*, 8, 8613, <https://doi.org/10.1038/s41598-018-26857-9>, 2018.
- 1075 Hosoda, S., Ohira, T., Sato, K., and Suga, T.: Improved description of global mixed-layer depth using Argo profiling floats, *J*
1076 *Oceanogr*, 66, 773–787, <https://doi.org/10.1007/s10872-010-0063-3>, 2010.
- 1077 Hunt, J. R.: Self-similar particle-size distributions during coagulation: theory and experimental verification, *J. Fluid Mech.*,
1078 122, 169, <https://doi.org/10.1017/S0022112082002158>, 1982.
- 1079 Ioannou, A., Speich, S., and Laxenaire, R.: Characterizing Mesoscale Eddies of Eastern Upwelling Origins in the Atlantic
1080 Ocean and Their Role in Offshore Transport, *Front. Mar. Sci.*, 9, 835260, <https://doi.org/10.3389/fmars.2022.835260>, 2022.
- 1081 Iversen, M. H. and Lampitt, R. S.: Size does not matter after all: No evidence for a size-sinking relationship for marine snow,
1082 *Progress in Oceanography*, 189, 102445, <https://doi.org/10.1016/j.pocean.2020.102445>, 2020.
- 1083 Jackson, G. A.: A model of the formation of marine algal flocs by physical coagulation processes, *Deep Sea Research Part A*.
1084 *Oceanographic Research Papers*, 37, 1197–1211, [https://doi.org/10.1016/0198-0149\(90\)90038-W](https://doi.org/10.1016/0198-0149(90)90038-W), 1990.
- 1085 Jackson, G. A. and Checkley, D. M.: Particle size distributions in the upper 100m water column and their implications for
1086 animal feeding in the plankton, *Deep Sea Research Part I: Oceanographic Research Papers*, 58, 283–297,
1087 <https://doi.org/10.1016/j.dsr.2010.12.008>, 2011.
- 1088 [Jouandet, M.-P., Jackson, G. A., Carlotti, F., Picheral, M., Stemmann, L., and Blain, S.: Rapid formation of large aggregates](https://doi.org/10.5194/bg-11-4393-2014)
1089 [during the spring bloom of Kerguelen Island: observations and model comparisons, *Biogeosciences*, 11, 4393–4406,](https://doi.org/10.5194/bg-11-4393-2014)
1090 <https://doi.org/10.5194/bg-11-4393-2014>, 2014.
- 1091 Kriest, I.: Different parameterizations of marine snow in a 1D-model and their influence on representation of marine snow,
1092 nitrogen budget and sedimentation, *Deep Sea Research Part I: Oceanographic Research Papers*, 49, 2133–2162,
1093 [https://doi.org/10.1016/S0967-0637\(02\)00127-9](https://doi.org/10.1016/S0967-0637(02)00127-9), 2002.

a mis en forme : Anglais (E.U.)

a mis en forme : Anglais (E.U.)

a mis en forme : Anglais (E.U.)

Code de champ modifié

- 1094 Lampitt, R. S., Noji, T., and Von Bodungen, B.: What happens to zooplankton faecal pellets? Implications for material flux,
 1095 Mar. Biol., 104, 15–23, <https://doi.org/10.1007/BF01313152>, 1990.
- 1096 [Laubscher, R. K., Perissinotto, R., and McQuaid, C. D.: Phytoplankton production and biomass at frontal zones in the Atlantic](#)
 1097 [sector of the Southern Ocean, Polar Biol, 13, https://doi.org/10.1007/BF00233138, 1993.](#)
- 1098 Laurenceau-Cornec, E., Trull, T., Davies, D., De La Rocha, C., and Blain, S.: Phytoplankton morphology controls on marine
 1099 snow sinking velocity, Mar. Ecol. Prog. Ser., 520, 35–56, <https://doi.org/10.3354/meps11116>, 2015.
- 1100 Laxenaire, R., Speich, S., Blanke, B., Chaigneau, A., Pegliasco, C., and Stegner, A.: Anticyclonic Eddies Connecting the
 1101 Western Boundaries of Indian and Atlantic Oceans, J. Geophys. Res. Oceans, 123, 7651–7677,
 1102 <https://doi.org/10.1029/2018JC014270>, 2018.
- 1103 Laxenaire, R., Speich, S., and Stegner, A.: Evolution of the Thermohaline Structure of One Agulhas Ring Reconstructed from
 1104 Satellite Altimetry and Argo Floats, J. Geophys. Res. Oceans, 124, 8969–9003, <https://doi.org/10.1029/2018JC014426>, 2019.
- 1105 Laxenaire, R., Speich, S., and Stegner, A.: Agulhas Ring Heat Content and Transport in the South Atlantic Estimated by
 1106 Combining Satellite Altimetry and Argo Profiling Floats Data, JGR Oceans, 125, e2019JC015511,
 1107 <https://doi.org/10.1029/2019JC015511>, 2020.
- 1108 Laxenaire, R., Guez, L., Chaigneau, A., Isic, M., Ioannou, A., and Speich, S.: TOEddies Global Mesoscale Eddy Atlas
 1109 Colocated with Argo Float Profiles, <https://doi.org/10.17882/102877>, 2024.
- 1110 Le Moigne, F. A. C.: Pathways of Organic Carbon Downward Transport by the Oceanic Biological Carbon Pump, Front. Mar.
 1111 Sci., 6, 634, <https://doi.org/10.3389/fmars.2019.00634>, 2019.
- 1112 Lehahn, Y., d’Ovidio, F., and Koren, I.: A Satellite-Based Lagrangian View on Phytoplankton Dynamics, Annu. Rev. Mar.
 1113 Sci., 10, 99–119, <https://doi.org/10.1146/annurev-marine-121916-063204>, 2018.
- 1114 Lévy, M., Franks, P. J. S., and Smith, K. S.: The role of submesoscale currents in structuring marine ecosystems, Nat Commun,
 1115 9, 4758, <https://doi.org/10.1038/s41467-018-07059-3>, 2018.
- 1116 Lima, I. D.: Biological response to frontal dynamics and mesoscale variability in oligotrophic environments: Biological
 1117 production and community structure, J. Geophys. Res., 107, 3111, <https://doi.org/10.1029/2000JC000393>, 2002.
- 1118 Llorc, J., Langlais, C., Matear, R., Moreau, S., Lenton, A., and Strutton, P. G.: Evaluating Southern Ocean Carbon Eddy-Pump
 1119 From Biogeochemical-Argo Floats, JGR Oceans, 123, 971–984, <https://doi.org/10.1002/2017JC012861>, 2018.
- 1120 Lutjeharms, J. R. E., Boebel, O., and Rossby, H. T.: Agulhas cyclones, Deep Sea Research Part II: Topical Studies in
 1121 Oceanography, 50, 13–34, [https://doi.org/10.1016/S0967-0645\(02\)00378-8](https://doi.org/10.1016/S0967-0645(02)00378-8), 2003.

a mis en forme : Anglais (E.U.)

a mis en forme : Anglais (E.U.)

a mis en forme : Anglais (E.U.)

Code de champ modifié

- 1122 Mahadevan, A.: The Impact of Submesoscale Physics on Primary Productivity of Plankton, *Annu. Rev. Mar. Sci.*, 8, 161–184,
 1123 <https://doi.org/10.1146/annurev-marine-010814-015912>, 2016.
- 1124 Mahadevan, A. and Archer, D.: Modeling the impact of fronts and mesoscale circulation on the nutrient supply and
 1125 biogeochemistry of the upper ocean, *J. Geophys. Res.*, 105, 1209–1225, <https://doi.org/10.1029/1999JC900216>, 2000.
- 1126 [Maier-Reimer, E., Mikolajewicz, U., and Winguth, A.: Future ocean uptake of CO2: interaction between ocean circulation and
 1127 biology., *Climate Dynamics*, 12, 711–722, <https://doi.org/10.1007/s003820050138>, 1996.](#)
- 1128 McCave, I. N.: Size spectra and aggregation of suspended particles in the deep ocean, *Deep Sea Research Part A. Oceanographic Research Papers*, 31, 329–352, [https://doi.org/10.1016/0198-0149\(84\)90088-8](https://doi.org/10.1016/0198-0149(84)90088-8), 1984.
- 1130 McGillicuddy, D. J.: Mechanisms of Physical-Biological-Biogeochemical Interaction at the Oceanic Mesoscale, *Annu. Rev. Mar. Sci.*, 8, 125–159, <https://doi.org/10.1146/annurev-marine-010814-015606>, 2016.
- 1132 McWilliams, J. C.: Submesoscale currents in the ocean, *Proc. R. Soc. A.*, 472, 20160117,
 1133 <https://doi.org/10.1098/rspa.2016.0117>, 2016.
- 1134 Møller, E. F., Borg, C. M. A., Jónasdóttir, S. H., Satapoomin, S., Jaspers, C., and Nielsen, T. G.: Production and fate of copepod
 1135 fecal pellets across the Southern Indian Ocean, *Mar Biol*, 158, 677–688, <https://doi.org/10.1007/s00227-010-1591-5>, 2011.
- 1136 Omand, M. M., D’Asaro, E. A., Lee, C. M., Perry, M. J., Briggs, N., Cetinić, I., and Mahadevan, A.: Eddy-driven subduction
 1137 exports particulate organic carbon from the spring bloom, *Science*, 348, 222–225, <https://doi.org/10.1126/science.1260062>,
 1138 2015.
- 1139 Penven, P., Lutjeharms, J. R. E., Marchesiello, P., Roy, C., and Weeks, S. J.: Generation of cyclonic eddies by the Agulhas
 1140 Current in the Lee of the Agulhas Bank, *Geophys. Res. Lett.*, 28, 1055–1058, <https://doi.org/10.1029/2000GL011760>, 2001.
- 1141 Picheral, M., Catalano, C., Brousseau, D., Claustre, H., Coppola, L., Leymarie, E., Coindat, J., Dias, F., Fevre, S., Guidi, L.,
 1142 Irisson, J. O., Legendre, L., Lombard, F., Mortier, L., Penkerch, C., Rogge, A., Schmechtig, C., Thibault, S., Tixier, T., Waite,
 1143 A., and Stemmann, L.: THE UNDERWATER VISION PROFILER 6: AN IMAGING SENSOR OF PARTICLE SIZE SPECTRA AND PLANKTON,
 1144 FOR AUTONOMOUS AND CABLED PLATFORMS, *Limnology & Ocean Methods*, 20, 115–129, <https://doi.org/10.1002/lom3.10475>,
 1145 2022.
- 1146 Picheral, M., Colin, S., Irisson, J-O.: EcoTaxa, a tool for the taxonomic classification of images, <http://ecotaxa.obs-vlfr.fr>
- 1147 Ploug, H., Iversen, M. H., and Fischer, G.: Ballast, sinking velocity, and apparent diffusivity within marine snow and
 1148 zooplankton fecal pellets: Implications for substrate turnover by attached bacteria, *Limnology & Oceanography*, 53, 1878–
 1149 1886, <https://doi.org/10.4319/lo.2008.53.5.1878>, 2008.

a mis en forme : Anglais (E.U.)

a mis en forme : Anglais (E.U.)

a mis en forme : Anglais (E.U.)

Code de champ modifié

1150 Prants, S. V.: Dynamical systems theory methods to study mixing and transport in the ocean, *Phys. Scr.*, 87, 038115,
1151 <https://doi.org/10.1088/0031-8949/87/03/038115>, 2013.

1152 Pujol, M.-I., Faugère, Y., Taburet, G., Dupuy, S., Pelloquin, C., Ablain, M., and Picot, N.: DUACS DT2014: the new multi-
1153 mission altimeter data set reprocessed over 20 years, *Ocean Sci.*, 12, 1067–1090, <https://doi.org/10.5194/os-12-1067-2016>,
1154 2016.

1155 Richardson, P. L., Lutjeharms, J. R. E., and Boebel, O.: Introduction to the “Inter-ocean exchange around southern Africa,”
1156 *Deep Sea Research Part II: Topical Studies in Oceanography*, 50, 1–12, [https://doi.org/10.1016/S0967-0645\(02\)00376-4](https://doi.org/10.1016/S0967-0645(02)00376-4),
1157 2003.

1158 Rodionov, S. N.: A sequential algorithm for testing climate regime shifts: ALGORITHM FOR TESTING REGIME SHIFTS,
1159 *Geophys. Res. Lett.*, 31, n/a-n/a, <https://doi.org/10.1029/2004GL019448>, 2004.

1160 Roquet, F., Madec, G., McDougall, T. J., and Barker, P. M.: Accurate polynomial expressions for the density and specific
1161 volume of seawater using the TEOS-10 standard, *Ocean Modelling*, 90, 29–43, <https://doi.org/10.1016/j.ocemod.2015.04.002>,
1162 2015.

1163 Sarmiento, J. L. and Gruber, N.: *Ocean biogeochemical dynamics*, Princeton University Press, Princeton, 503 pp., 2006.

1164 Schmid, C., Boebel, O., Zenk, W., Lutjeharms, J. R. E., Garzoli, S. L., Richardson, P. L., and Barron, C.: Early evolution of
1165 an Agulhas Ring, *Deep Sea Research Part II: Topical Studies in Oceanography*, 50, 141–166, [https://doi.org/10.1016/S0967-
1166 0645\(02\)00382-X](https://doi.org/10.1016/S0967-0645(02)00382-X), 2003.

1167 Ser-Giacomi, E., Baudena, A., Rossi, V., Follows, M., Clayton, S., Vasile, R., López, C., and Hernández-García, E.:
1168 Lagrangian betweenness as a measure of bottlenecks in dynamical systems with oceanographic examples, *Nat Commun*, 12,
1169 4935, <https://doi.org/10.1038/s41467-021-25155-9>, 2021.

1170 Shadden, S. C., Lekien, F., and Marsden, J. E.: Definition and properties of Lagrangian coherent structures from finite-time
1171 Lyapunov exponents in two-dimensional aperiodic flows, *Physica D: Nonlinear Phenomena*, 212, 271–304,
1172 <https://doi.org/10.1016/j.physd.2005.10.007>, 2005.

1173 Shanks, A. L. and Trent, J. D.: Marine snow: sinking rates and potential role in vertical flux, *Deep Sea Research Part A. Oceanographic Research Papers*, 27, 137–143, [https://doi.org/10.1016/0198-0149\(80\)90092-8](https://doi.org/10.1016/0198-0149(80)90092-8), 1980.

1175 Shih, Y., Hung, C., Tuo, S., Shao, H., Chow, C. H., Muller, F. L. L., and Cai, Y.: The Impact of Eddies on Nutrient Supply,
1176 Diatom Biomass and Carbon Export in the Northern South China Sea, *Front. Earth Sci.*, 8, 537332,
1177 <https://doi.org/10.3389/feart.2020.537332>, 2020.

1178 Siegel, D. A., Buesseler, K. O., Doney, S. C., Sailley, S. F., Behrenfeld, M. J., and Boyd, P. W.: Global assessment of ocean
1179 carbon export by combining satellite observations and food-web models, *Global Biogeochemical Cycles*, 28, 181–196,
1180 <https://doi.org/10.1002/2013GB004743>, 2014.

1181 Siegelman, L., Klein, P., Rivière, P., Thompson, A. F., Torres, H. S., Flexas, M., and Menemenlis, D.: Enhanced upward heat
1182 transport at deep submesoscale ocean fronts, *Nat. Geosci.*, 13, 50–55, <https://doi.org/10.1038/s41561-019-0489-1>, 2020.

1183 Soviadan, Y. D., Beck, M., Habib, J., Baudena, A., Drago, L., Accardo, A., Laxenaire, R., Speich, S., Brandt, P., Kiko, R., and
1184 Stemmann, L.: Marine snow morphology drives sinking and attenuation in the ocean interior,
1185 <https://doi.org/10.5194/egusphere-2024-3302>, 7 November 2024.

1186 Stammer, D.: Global Characteristics of Ocean Variability Estimated from Regional TOPEX/POSEIDON Altimeter
1187 Measurements, *J. Phys. Oceanogr.*, 27, 1743–1769, [https://doi.org/10.1175/1520-0485\(1997\)027<1743:GCOOVE>2.0.CO;2](https://doi.org/10.1175/1520-0485(1997)027<1743:GCOOVE>2.0.CO;2),
1188 1997.

1189 Stemmann, L. and Boss, E.: Plankton and Particle Size and Packaging: From Determining Optical Properties to Driving the
1190 Biological Pump, *Annu. Rev. Mar. Sci.*, 4, 263–290, <https://doi.org/10.1146/annurev-marine-120710-100853>, 2012.

1191 [Stemmann, L., Gorsky, G., Marty, J.-C., Picheral, M., and Miquel, J.-C.: Four-year study of large-particle vertical distribution
1192 \(0–1000m\) in the NW Mediterranean in relation to hydrology, phytoplankton, and vertical flux, *Deep Sea Research Part II:
1193 Topical Studies in Oceanography*, 49, 2143–2162, \[https://doi.org/10.1016/S0967-0645\\(02\\)00032-2\]\(https://doi.org/10.1016/S0967-0645\(02\)00032-2\), 2002.](#)

1194 Stemmann, L., Jackson, G. A., and Ianson, D.: A vertical model of particle size distributions and fluxes in the midwater column
1195 that includes biological and physical processes—Part I: model formulation, *Deep Sea Research Part I: Oceanographic Research
1196 Papers*, 51, 865–884, <https://doi.org/10.1016/j.dsr.2004.03.001>, 2004.

1197 [Stemmann, L., Prieur, L., Legendre, L., Taupier-Letage, I., Picheral, M., Guidi, L., and Gorsky, G.: Effects of frontal processes
1198 on marine aggregate dynamics and fluxes: An interannual study in a permanent geostrophic front \(NW Mediterranean\), *Journal
1199 of Marine Systems*, 70, 1–20, <https://doi.org/10.1016/j.jmarsys.2007.02.014>, 2008.](#)

1200 [Stukel, M. R., Aluwihare, L. I., Barbeau, K. A., Chekalyuk, A. M., Goericke, R., Miller, A. J., Ohman, M. D., Ruacho, A.,
1201 Song, H., Stephens, B. M., and Landry, M. R.: Mesoscale ocean fronts enhance carbon export due to gravitational sinking and
1202 subduction, *Proc. Natl. Acad. Sci. U.S.A.*, 114, 1252–1257, <https://doi.org/10.1073/pnas.1609435114>, 2017.](#)

1203 Tarry, D. R., Essink, S., Pascual, A., Ruiz, S., Poulain, P., Özgökmen, T., Centurioni, L. R., Farrar, J. T., Shcherbina, A.,
1204 Mahadevan, A., and D’Asaro, E.: Frontal Convergence and Vertical Velocity Measured by Drifters in the Alboran Sea, *J.
1205 Geophys. Res. Oceans*, 126, <https://doi.org/10.1029/2020JC016614>, 2021.

1206 [Thomalla, S. J., Fauchereau, N., Swart, S., and Monteiro, P. M. S.: Regional scale characteristics of the seasonal cycle of
1207 chlorophyll in the Southern Ocean, *Biogeosciences*, 8, 2849–2866, <https://doi.org/10.5194/bg-8-2849-2011>, 2011.](#)

a mis en forme : Anglais (E.U.)

a mis en forme : Anglais (E.U.)

a mis en forme : Anglais (E.U.)

Code de champ modifié

a mis en forme : Anglais (E.U.)

a mis en forme : Anglais (E.U.)

a mis en forme : Anglais (E.U.)

Code de champ modifié

a mis en forme : Anglais (E.U.)

a mis en forme : Anglais (E.U.)

Code de champ modifié

a mis en forme : Anglais (E.U.)

a mis en forme : Anglais (E.U.)

a mis en forme : Anglais (E.U.)

Code de champ modifié

- 1208 Thomas, L. N., Tandon, A., and Mahadevan, A.: Submesoscale processes and dynamics, in: Geophysical Monograph Series,
 1209 vol. 177, edited by: Hecht, M. W. and Hasumi, H., American Geophysical Union, Washington, D. C., 17–38,
 1210 <https://doi.org/10.1029/177GM04>, 2008.
- 1211 Trudnowska, E., Lacour, L., Ardyna, M., Rogge, A., Irisson, J. O., Waite, A. M., Babin, M., and Stemmann, L.: Marine snow
 1212 morphology illuminates the evolution of phytoplankton blooms and determines their subsequent vertical export, Nat Commun,
 1213 12, 2816, <https://doi.org/10.1038/s41467-021-22994-4>, 2021.
- 1214 Turner, J. T.: Zooplankton fecal pellets, marine snow, phytodetritus and the ocean’s biological pump, Progress in
 1215 Oceanography, 130, 205–248, <https://doi.org/10.1016/j.pocean.2014.08.005>, 2015.
- 1216 Waite, A. M., Stemmann, L., Guidi, L., Calil, P. H. R., Hogg, A. M. C., Feng, M., Thompson, P. A., Picheral, M., and Gorsky,
 1217 G.: The wineglass effect shapes particle export to the deep ocean in mesoscale eddies, Geophysical Research Letters, 43, 9791–
 1218 9800, <https://doi.org/10.1002/2015GL066463>, 2016.
- 1219 [Williams, J. R. and Giering, S. L. C.: In Situ Particle Measurements Deemphasize the Role of Size in Governing the Sinking](#)
 1220 [Velocity of Marine Particles, Geophysical Research Letters, 49, e2022GL099563, https://doi.org/10.1029/2022GL099563,](#)
 1221 [2022.](#)
- 1222 Wunsch, C.: Where do ocean eddy heat fluxes matter?, J. Geophys. Res., 104, 13235–13249,
 1223 <https://doi.org/10.1029/1999JC900062>, 1999.
- 1224 Yeo, I.-K.: A new family of power transformations to improve normality or symmetry, Biometrika, 87, 954–959,
 1225 <https://doi.org/10.1093/biomet/87.4.954>, 2000.

a mis en forme : Anglais (E.U.)

a mis en forme : Anglais (E.U.)

a mis en forme : Anglais (E.U.)

Code de champ modifié

a mis en forme : Espace Après : 0 pt

a supprimé: ¶